BULLETIN OF MATERIALS SCIENCE AND METALLURGY

Volume 1 I Issue 3 I Pages 1-30 I 2024

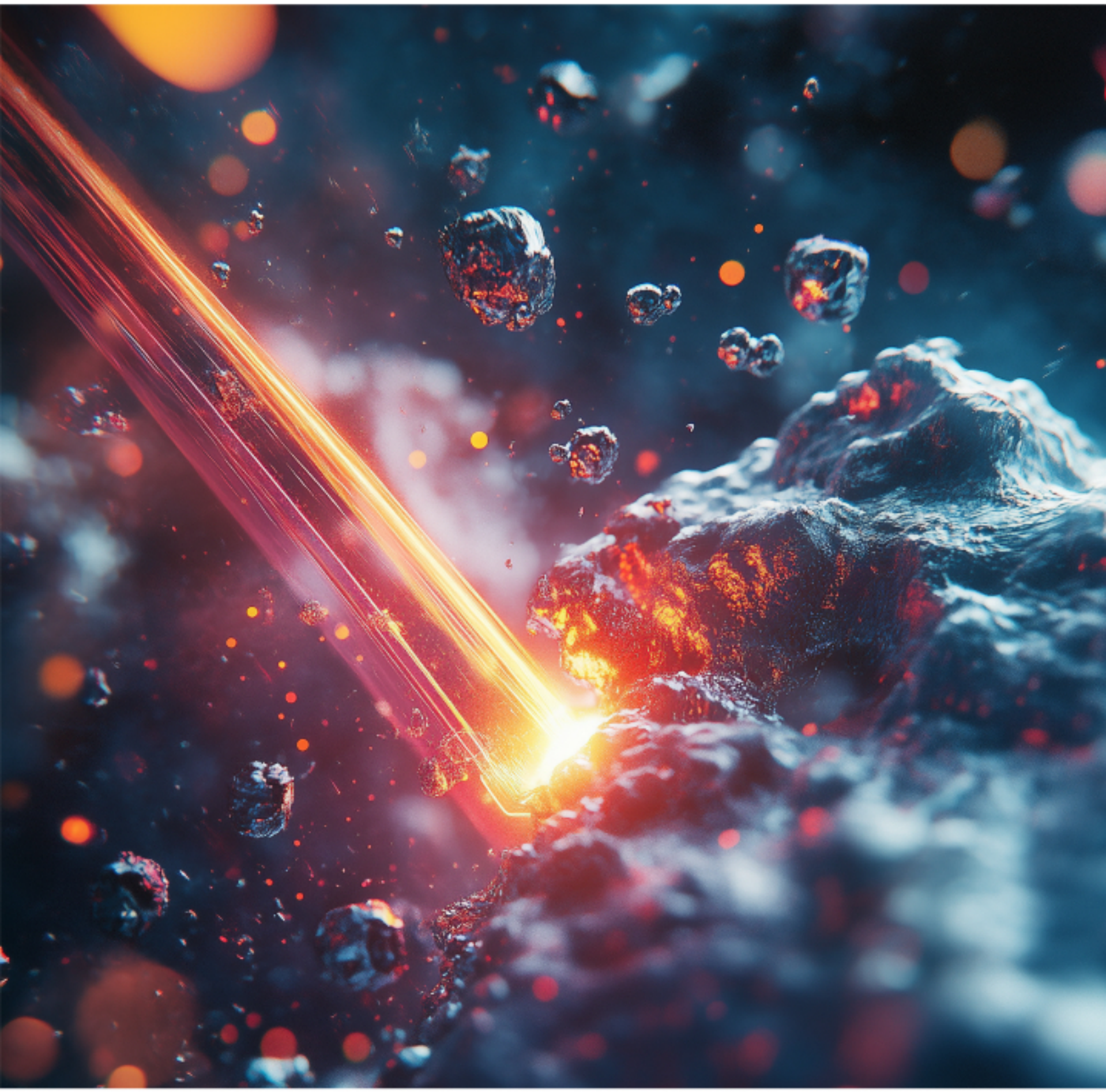

ONLINE ISSN:3023-6509

bulletinofmsm.org/

BULLETIN OF MATERIALS SCIENCE AND METALLURGY

BULLETIN OF MATERIALS SCIENCE AND METALLURGY

BULLETIN OF MATERIALS SCIENCE AND METALLURGY

BULLETIN OF
MATERIALS SCIENCE AND METALLURGY

CONTENTS

Effect of Intensive Milling on The Structural Characteristics of Shale Ore
Turan Uysal,* Hikmet Sis, Murat Erdemoğlu
Page: 1 - 6

Laser Welding of Aluminum to Copper: Properties of The Welded Joints and Optimization of Parameters
Fatih Şahin, Emel Taban
Page: 7 - 15

Investigation of The Effect Of Thermo-Mechanical Processing Orientation On The Final Material Performance In 6xxx Aluminium Alloys Produced with High Recycling Rates
Zeynep Tutku Ozen*, Irem Yaren Siyah, Ilyas Artunc Sari, Melih Caylak,
Gorkem Ozcelik, Burak Kardesler, Ibrahim Bat
Page: 16 - 19

Effects of Alkali Ratios on Alkali Barium Glasses for Compression Sealing
Tutku Turgutlugil Gökçe*, M. Kaan Pehlivanoğlu, Abdullah Öztürk
Page: 20 - 24

Effect of Aluminum Content on The Properties of Spark Plasma Sintered Tungsten, Niobium, Vanadium, Molybdenum & Aluminum Refractory High Entropy Alloys
Erman Yaman*, Duygu Ağaoğulları, M.Lütfi Öveçoğlu
Page: 25 - 30

BMSM

Bulletin of Materials Science & Metallurgy

Periodical Scientific Journal of UCTEA Chamber of Metallurgical and Materials Engineers

Volume 1, Issue 3, 2024, Pages 1-6 Received: 07 November 2024 Accepted: 25 December 2024

https://doi.org/10.70342/VFYD5509

Research Article

Effect of intensive milling on the structural characteristics of shale ore

Turan Uysal[a,*], Tufan Kıyak[b], Hikmet Sis[b], Murat Erdemoğlu[b]

[a]Gümüşhane University, Mining Engineering Department, Gümüşhane, Turkiye

[b]İnönü University, Mining Engineering Department, Malatya, Turkiye

*Corresponding author's email: turanuysal@gumushane.edu.tr

Abstract

This investigation examined the effect of intensive milling on the structural properties of shale ore with high Rare Earth Element (REE) content, which is unsuitable for aluminum production due to high silica and/or low aluminum. In this context, bauxite-related shale ore from the Karaman province in Türkiye was subjected to intensive milling under various conditions. Representative samples were collected from the deposit were first subjected to coarse crushing and milling processes, and then were excessively milled in a planetary ball mill under different conditions to ensure their mechanical activation. Changes occurred during milling were examined by XRD, TGA, BET and SEM analysis. The characterization results of intensively milled and unmilled samples showed that the intensive-milled samples were mechanically activated. As a result, the usability of mechanically activated shale for the recovery of Al and REEs from shale ore was evaluated.

Keywords

Shale; Rare earth element; Milling; Mechanical activation

1. Introduction

The mechanical activation of minerals increases the selective dissolution and solvent efficiencies during leaching, leading to an increase in the reaction rate [1]. This increase occurs as a result of an increase in the specific surface area and structural disorder [2], an increase in microstress [3], amorphization of mineral crystals [4], microtopographic changes [5], the formation of new phases more prone to dissolution [6], and a tendency for thermal reduction [7]. In the case of mechanical activation, the mineral behaves more actively during metallurgical processes such as calcination [8], roasting [9], or leaching [10], which reduces the temperature of the process or increases its speed.

In mechanically activated materials, the plastic deformation and irregularity of the crystal structure, that is, the formation of lattice distortion, lattice defects, and dislocation density, increase. Thus, the crystal structure becomes amorphous with intensive milling. In this case, displacement of the XRD diffraction peaks of the minerals was observed as broadening, shortening, or disappearance of the peaks.

Rare Earth Elements (REEs) are indispensable to modern materials and energy technologies. REEs are widely used in the production of many high-tech devices and equipment, such as electric/hybrid vehicles, wind turbines, solar panels, aircraft, and electronic devices, such as cell phones, computers, rechargeable batteries, and modern medical devices, such as MRI devices [11]. In particular, the demand for REEs (Nd, Pr, Tb, and Dy) used in magnet production is expected to increase, and the supply of these elements is expected to be problematic as of 2025. Therefore, countries have sought to produce REE from secondary geological sources such as ionic clays, red mud and bauxite-related shales with low U and Th content [12-13].

The Kızıldağ bauxite mineralization in Türkiye are situated within the Bolkar Mountain Bauxite Province. The protolith, or source rocks, of the Bolkar Mountain bauxite mineralization was identified as shale by Hanilçi [14]. Heavy REE

enrichment is characteristic of these deposits, and bauxite deposits, along with their source rocks and shales, contain significant concentrations of REEs that may serve as potential sources. Researchers [15-18] have investigated the formation of REE in bauxite-related deposits in the Bolkar mountain region and determined that clay minerals formed during the lateritic weathering process compensate for the lack of electrostatic charge on their outer edges with ions, such as Ca^{2+}, Na^{+}, and REE^{3-}. Consequently, REEs were enriched through adsorption on the outer surface of the clay. These REE-rich clays were subsequently formed by the addition of bauxite [2].

Mechanical activation, the mineral behaves more actively during metallurgical processes such as roasting [9] or leaching [10] which reduces the temperature of the process or increases its speed. In this context, Kızıldağ shale ore was intensively milled before the acidic leaching. The intensively milled ore was characterized using different characterization methods, and the effect of intensive milling was investigated.

2. Materials and Methods

In this study, shale ore was selected in a representative piece size from the mines that belong to the Demireller Mining company. The shale ore was systematically crushed for size reduction. The crushing process was carried out gradually with a Pulverisette I model (Fritsch) jaw crusher with adjustable outlet opening to a length of -4,75 mm, and one half of the crushed material was saved as witness sample. The other half was crushed further with a jaw crusher to -2 mm.

2.1. Characterization of the ore

X-ray diffraction (XRD) analyses were used to determine the mineral composition of Kızıldağ shale ore and intensively milled products, and to monitor the changes in the crystal properties of these minerals with milling. For this purpose, XRD patterns were obtained using a Rigaku MiniFlex 600 model XRD instrument (Munzur University) at CuKα (α: 1.5405 Å) irradiance, 2°/min scanning speed and diffraction angles ranging from 5-80º. A scanning electron microscope (SEM), Hitachi SU3500 model (Munzur University), was used to determine the micromorphological properties. BET surface area measurements were performed using a Micromeritics TriStar II Plus model surface area measuring system in a liquid nitrogen environment based on the N_2 gas adsorption technique. Perkin Elmer Elan 9000 model ICP-MS and ICP-AES instruments (ALS Labs) were used to determine the chemical content of the ore samples.

2.2. Milling of ore for mechanical activation

For mechanical activation, intensive-milling processes were carried out in a Fritsch Pulverisette 6 model mono-shaft planetary ball mill (İnönü University). The milling process was carried out in an air-cooled planetary ball mill with high energy efficiency, using a tungsten carbide mortar with an internal volume of 250 cm^3 and 10 mm diameter balls made of the same material as the mortar. The milling was carried out dry at milling speeds of 400 and 500 rpm, at ball-to-powder ratios (BPR) of 5, 10, and 20 by mass and for different durations ranging from 15 to 90 minutes.All samples were dried at 105 °C for at least 1 hour to remove surface moisture prior to milling and then cooled in a desiccator. To prevent overheating of the mill, the mill was programmed to run for 10 minutes followed by a 10 minute hold programme for cooling to complete the required milling time.

For evaluation of the milling intensity and planetary mill efficiency, the specific milling work or stress energy, SE ($J.kg^{-1}$) [19], was calculated using the Eq. 1.

$$SE\ (J.kg^{-1}) = (m_B/m_S) \cdot a \cdot n \cdot t_M \cdot D \qquad \text{(Eq. 1)}$$

where m_B, m_0, a, n, t_M and D refer to mass of milling media (kg), mass of material charge (kg), theoretical acceleration in the center of the bowl in the planetary mill (m/s^2), speed of the planetary mill (1/s), milling time (s) and inner mill diameter (m), respectively. Theoretical acceleration for the planetary ball mill is 26.41 m/s^2, as given by the supplier. With the help of data obtained by XRD analysis, crystalline state of the samples was calculated using Eq. 2. Effect of mechanical activation was evaluated by a mass fraction of the crystalline phase (X) in the milled sample. X was compared with the reference substance (unmilled substance) which is assumed to correspond to 100% crystalline [20]. Thus, it holds that,

$$\text{Degree of Crystallinity (X), \%} = (U_o I_x / I_o U_x) * 100 \qquad \text{(Eq. 2)}$$

where U_0 and U_X denote the backgrounds of unmilled (reference) sample and milled sample, while I_0 and I_X are integral intensities of diffraction lines of the mineral in the unmilled (reference) sample and milled sample, respectively. Accordingly, if $I_X = I_0$, it is interpreted that the mineral is 100% XRD crystalline or 0% XRD amorphous with respect to the diffraction surface (hkl) to which the peak belongs. The equation is based on the assumption that the mechanical activation is not accompanied by a texture error (e.g., due to preferential orientation where there was none in the unmilled sample). Complementary value of amorphization (A) (also called degree of amorphization or content of X-ray amorphous phase) can also be used. The degree of amorphization is found by subtracting 100 from the degree of crystallization (X).

3. Results and Discussion

3.1. Chemical properties

The chemical composition of bauxite-related shales is presented in Table 1 and Table 2. XRD analysis method was

used to determine the mineralogical content of Kızıldağ shale ore (Figure 1).

Table 1. Oxide content (%) of Kızıldağ shale ore determined by ICP-AES.

SiO_2	Al_2O_3	Fe_2O_3	CaO	MgO	Na_2O	K_2O	TiO_2	LOI
42.7	28.8	4.29	5.69	0.56	3.04	3.04	1.41	9.49

Table 2. REE content (ppm) of Kızıldağ shale ore determined by ICP-MS.

Ce	La	Y	Nd	Sc	Pr	Dy	Er	Gd	Sm
115.7	82.8	83.8	59.2	28	15.7	11.65	7.46	10.42	10.75
Yb	**Ho**	**Lu**	**Eu**	**Tb**	**Tm**	**∑REE**	**Rb**	**Th**	**U**
7.06	2.52	1.04	1.88	1.73	1.09	441.5	112	21.7	4.39

As a result of ICP-AES analysis in Table 1, Kızıldağ shale ore has an average content of 42.70% SiO_2 and 28.8% Al_2O_3. In the literature, it is stated that ionic clays contain approximately 500-3,000 ppm REE [15]. In Table 2, the total REE content was determined as 441.5 ppm, and it was found to have a low content compared to other studies on this deposit. Although it is low, it has the quality that can be evaluated within the limit grade. In the study conducted by Hepvidinli [15], it was stated that the REE content of Kızıldağ ore varies between 240-3,000 ppm. It is evaluated that this variability may be due to the formation of REE minerals such as allanite and serite in different regions of Kızıldağ region.

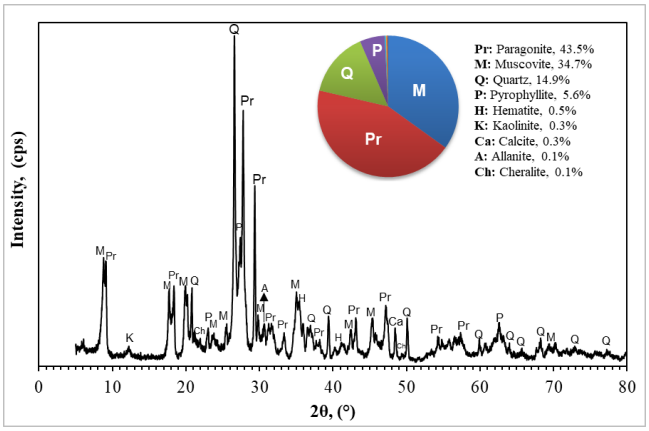

Figure 1. XRD pattern of Kızıldağ shale ore and its contents determined by Rietveld analysis (M: Muscovite, P: Pyrophyllite, Pr: Paragonite, Q: Quartz, K: Kaolinite, H: Hematite).

As analyzed by X-ray diffractometer (Fig. 1), the ore contains mainly paragonite ($NaAl_3Si_3O_{10}(OH)_2$, ICDD PDF# 24-1047), muscovite ($KAl_3Si_3O_{10})(OH)_2$; ICDD PDF# 07-0042), quartz (SiO_2; ICDD PDF# 46-1045), pyrophyllite ($Al_2Si_4O_{10}(OH)_2$; ICDD PDF# 46-1308), kaolinite ($Al_2Si_2O_5(OH)_4$; ICDD PDF# 29-1488), and hematite (Fe_2O_3; ICDD PDF# 80-5406).

3.2. XRD analysis of intensive-milled ore

XRD changes of the ore milled at 400 rpm mill speed, BPR: 10, 20 ratio and different milling times are given in Figure 2a-b. XRD patterns of the ore milled at 500 rpm mill speed for various times in Figure 3.

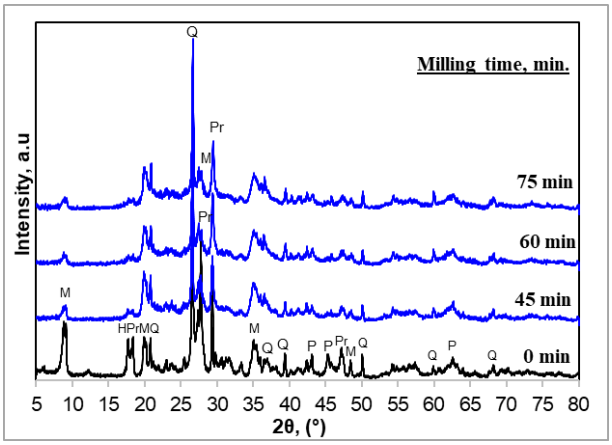

(a. BPR: 10)

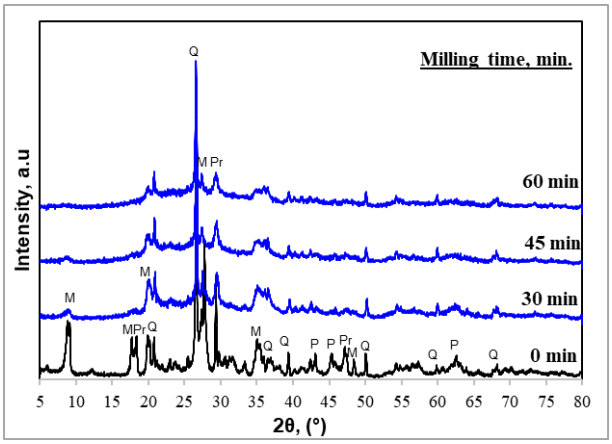

(b. BPR: 20)

Figure 2. XRD patterns of the ore milled at 400 rpm mill speed for various times (P: Pyrophyllite, Pr: Paragonite, M: Muscovite, C: Calcite, Q: Quartz).

Figure 2a shows that at all milling times, the peak intensities of profillite, paragonite and muscovite minerals slightly decreased compared to the unmilled sample. No significant change was observed with increasing milling time. Figure 2b shows the muscovite at 2θ: 9.52º decreased significantly at 30 and 45 minutes and disappeared completely at 60 minutes of milling time. The muscovite peak at 18,34º disappeared completely at 45 minutes of milling time. At 2θ: 35,06º, it is

observed that the peak broadens due to amorphization and the broadening increases as the milling time increases.

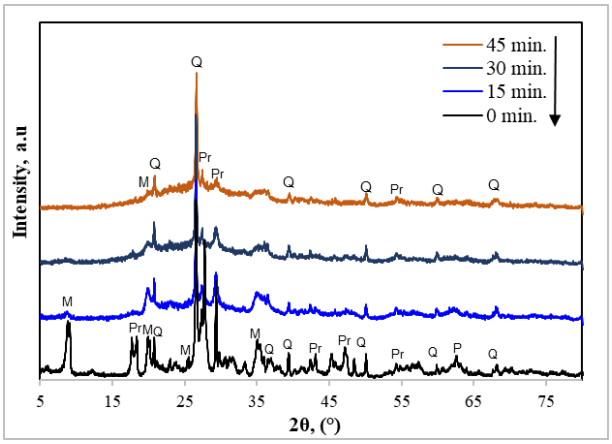

Figure 3. XRD patterns of the ore milled at 500 rpm mill speed for various times (Pr: Paragonite, M: Muscovite, Q: Quartz, P: Pyrophyllite, K: Kaolinite).

Upon examination of Fig. 3, it is evident that the peak intensities of the minerals decreased across all milling times. Only quartz, muscovite, and paragonite peaks remained discernible in the XRD pattern after 45 min of milling. Peaks associated with clay minerals such as pyrophyllite, paragonite, kaolinite, and halloysite were no longer detectable. Furthermore, it was observed that the muscovite peak at 2θ: 35.06° broadened because of amorphization, with the broadening increasing proportionally to the milling time. The peak intensities diminished more rapidly at 500 rpm milling speed compared to 400 rpm, indicating that mechanical activation was achieved in shorter durations at higher milling speeds. In addition, it is observed that the peaks disappear, and their intensity decreases in shorter periods at 500 rpm milling compared to 400 rpm milling speed. Thus, it is anticipated that activation can be realized in a shorter time at high milling speed.

Based on the XRD analysis data of the milled ores, the degree of amorphization of paragonite (2θ: 29.34°), quartz (2θ: 26.55°) and muscovite (2θ: 27.73°) in the ore was calculated. The variation of amorphization degrees of paragonite, muscovite and quartz minerals with milling time at a constant milling speed of 500 rpm and a constant ball to ore ratio of 20 is presented in Fig. 4.

It is seen that Fig. 4, in general, paragonite and muscovite have a high degree of amorphization while quartz has a significantly lower degree of amorphization. There is also an increasing trend in amorphization with milling time for all three minerals. It can also be seen that the amorphization degree of quartz is over 50% because of intensive milling. Considering the leaching efficiency, it is desirable that the quartz amorphized as little as possible to prevent the gelation of silica during the acid leaching.

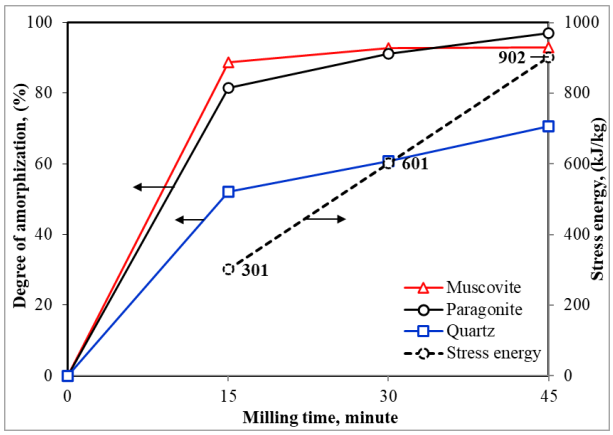

Figure 4. Variation of the degree of amorphization of paragonite, muscovite and quartz with milling time (500 rpm, BPR: 20).

3.3. SEM analysis of milled ore

The surface morphology of the intensive-milled products was examined with the help of SEM and the images obtained are given in Figure 5.

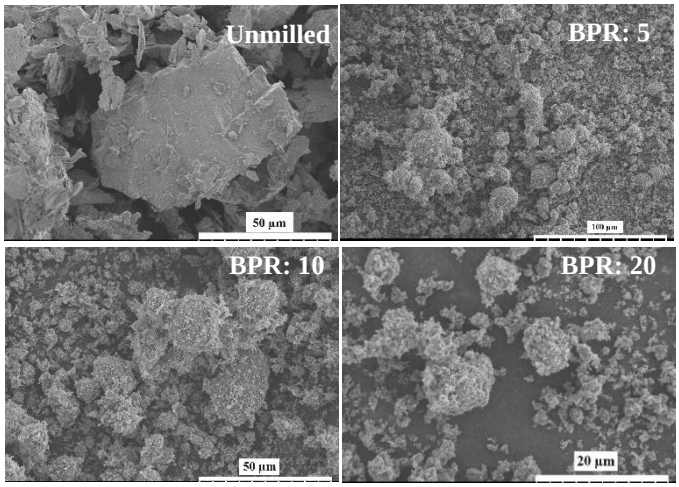

Figure 5. SEM images of unmilled and ore milled at 400 rpm, 45 min, BPR: 5-10-20 condition.

The layered/leaf-like structured particles shown in Fig. 5 unmilled ore considered clay minerals. The prismatic structured particle observed in Fig. 5 unmilled was also confirmed to be paragonite by XRD analysis. The spherical particles in Figure 5 400 rpm, 45 min, BPR: 5-10-20 condition are believed to be agglomerates comprising minerals with low hardness in the ore. In general, it was observed in SEM micrographs that the particle size of agglomerates decreased as the milling conditions became more severe. From the SEM microphotographs, it was seen that the particle sizes of the agglomerates decreased as the milling conditions became more intense.

3.4. BET surface area analysis

Surface area (SA) of unmilled and milled pyrophyllite samples were determined by BET surface area measurement based on nitrogen adsorption technique. Fig. 6 shows change of BET SA of milled shale with milling time.

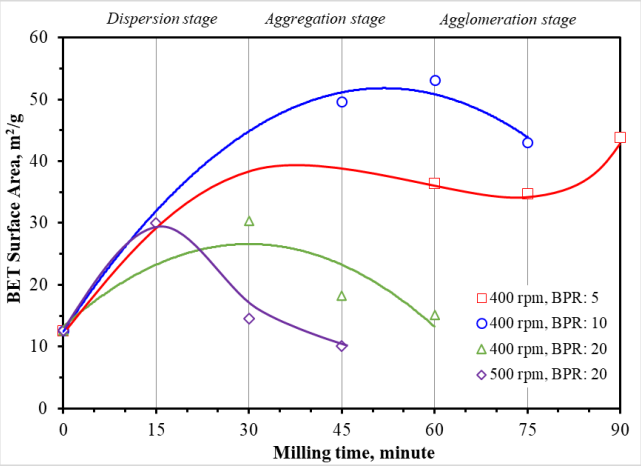

Figure 6. Change in BET specific surface area of shale ore milled at different BPR values and 400-500 rpm milling speed for different times.

According to the BET surface area analysis results, the ore is brittle and with milling the BET specific surface area increases from about 13 m^2/g to 55 m^2/g (Figure 6). As the milling time increases, an increase in BET surface area is observed in the dispersion phase and a general decrease is observed in the aggregation and agglomeration phases. During the aggregation and agglomeration phases, the surface area generally decreases due to the increase in agglomeration. At BPR: 5, an increase, then a decrease and again an increase is observed with increasing milling time. BPR: 10 is the milled product with the highest surface area compared to the others, and a parabolic increase was observed up to 60 minutes, and then a sharp decrease was observed in the agglomeration phase. It can be seen that the surface area of the shale ore increases up to 30 minutes at BPR: 20, but the surface area decreases after this period. BET specific surface area as a function of BPR except for BPR: 5, a decrease is observed after an increase up to a certain level. The reason for this is that the agglomeration effect of the ore particles occurs after a period of milling, as determined by SEM analysis of the milled ore.

3.5. TG analysis of intensively milled ore

Thermogravimetric analysis (TGA) curves of the ore samples milled at 400 rpm are shown in Figure 7 for different milling times (15-90 minutes) and compared. The maximum mass loss is around 6%, with a sharp decrease in the dehydroxylation zone between 470-750 °C, which is the most significant. This mass loss should be the indication of the disintegration of the hydrated structure, the occurrence of dehydration and dehydroxylation reactions, and the subsequent movement of interlayer water.

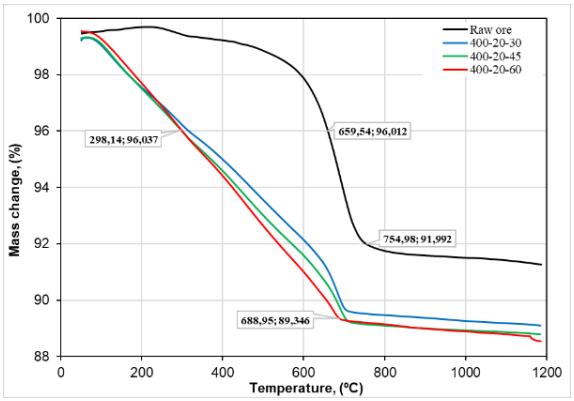

Figure 7. TGA curves of samples unmilled and milled at different times at 400 rpm mill speed.

The first notable finding in Figure 7 is that dehydroxylation, which is known to occur characteristically in the 550-800 °C temperature range in unmilled ores [21], starts at lower temperatures in milled ores. As milling time increases, mass loss increases. This is due to the formation of new surfaces and their influence by temperature. At 400 rpm, it was observed that the TGA curve shifted to the left due to the effect of intensive milling at all BPR, i.e. thermal changes occurred at lower temperatures.

It was also observed that the curves shifted more to the left up to BPR: 20 at a milling speed of 400 rpm. While the sharp point in the curve where mass loss decreases and dehydroxylation is largely complete was reached at 754.98 ºC with 8.01% mass loss in the raw ore, it was reached at 688.95 ºC with 10.65% mass loss in the intensive milled ore at 400-20-60 (rpm-BPR-time). In other words, at this point, a difference of 66.03 ºC and 2.64% occurred due to the effect of transformation (left shift) as a result of intensive milling. On the other hand, it can be seen that the mass loss after approximately 730 ºC as a result of milling for 45 minutes at a milling speed of 500 rpm at a ratio of BPR: 20 is even lower than that of the ore. While the mass loss of the fresh ore was 8.73%, the mass loss of the ore milled at 500-20-45 was 7.98%. This is due to the loss of water (dehydroxylation) in the crystalline structure in the mill during intensive milling.

4. Conclusion

In this study, shale ore containing mainly pyrophyllite, muscovite and quartz was mechanically activated by intensive milling to increase the leaching recovery. The effects of intensive milling on the structural properties of the ore and the thermal transformations during heating were investigated. In

general, pyrophyllite and muscovite were found to have a high degree of amorphization, whereas quartz had a significantly lower degree of amorphization. As a result of milling for 30 minutes, pyrophyllite and muscovite minerals were found to be over 80% amorphous, while quartz was 40% amorphous. SEM analysis showed that the particles were agglomerated, a typical result of intensive milling. According to the TG curves, dehydration and dehydroxylation occur at lower temperatures as BPR and milling speed increase, clearly showing the effect of mechanical activation. Based on all these results, it was concluded that the ore was mechanically activated. As a result, mechanically activated ore behaves more actively in the leaching process.

Declaration of Competing Interest

The authors declare that they have no known competing financial interests or personal relationships that could have appeared to influence the work reported in this paper.

Acknowledgement

The authors thank the Scientific and Technological Research Council of Turkey (TÜBİTAK) for financially supporting this study via Project No 122M810, Demireller Mining Inc. for providing shale ore samples from Ayrancı (Karaman, Turkey).

CRediT authorship contribution statement

Turan Uysal: Investigation, Validation, Formal analysis, Writing-original draft. ORCİD ID: 0000-0003-1643-6725

Tufan Kıyak: Investigation, Validation. ORCİD ID: 0000-0002-5438-3794

Hikmet Sis :Conceptualization, Writing-review & editing, Supervision. ORCİD ID: 0000-0001-8840-5448

Murat Erdemoğlu: Data curation, Writing-review & editing, Supervision. ORCİD ID: 0000-0003-2922-7965

References

[1] C.J., Warris, P.G., McCormick, Mechanochemical processing of refractory pyrite. Minerals Engineering, 10, (1997), 1119-1125.
[2] P., Baláž, Influence of solid state properties on ferric chloride leaching of mechanically activated galena. Hydrometallurgy, 40, (1996), 359-368.
[3] P., Baláž, Extractive Metallurgy of Activated Minerals, Amsterdam: Elsevier, (2000).
[4] T., Uysal, Investigation of activation conditions in alumina production from pyrophyllite ore by acid leaching method. PhD Thesis, Inonu University, Mining Engineering Department, (2018), Malatya, Türkiye.
[5] D., Tromans, J.A., Meech, Enhanced dissolution of minerals: microtopography and mechanical activation. Miner. Eng. 12, (1999), 609-625.
[6] N.J., Welham, Enhanced dissolution of tantalite/columbite following milling. Int. J. Miner. Process., 61, (2001), 145-154.
[7] N.J., Welham, Activation of the carbothermic reduction of manganese ore. Int. J. Miner. Process., 67, (2002), 187-198.
[8] M., Şener, T., Uysal, M. Erdemoğlu, Economic Evaluation of Thermal and Mechanical Activation Energies in Gypsum Production. Sci. Min. J., 63, (2024), Issue: 1, 47 - 52.
[9] B., Alyousif, T., Uysal, M.K., Aydemir, M. Erdemoğlu, Contribution of mechanical activation for obtaining potassium chloride from microcline. Min. Metall. Explor. 40, 4, (2023) 1311- 1319.
[10] M., Erdemoğlu, M., Birinci, T., Uysal, E., Porgalı, T.S., Barry, Acid leaching performance of mechanically activated pyrophyllite ore for Al_2O_3 extraction. J. Mater. Sci. 53, (2018), 13801-13812.
[11] N., Krishnamurthy, C. K. Gupta, Extractive Metallurgy of Rare Earths (Second Edition), (2016) CRC Press-Taylor & Francis Group.
[12] H., Öztürk, N., Hanilçi, S., Altuncu, C. Kasapçı, Rare earth element (REE) resources of Turkey: an overview of their characteristics and origin, Mineral Res. Expl. Bul., (2019) 159 143-129.
[13] E.C., Ünal, M., Karacahan, T., Uysal, Hydrometallurgical roadmaps and future strategies for recovery of rare earth elements. Miner. Process. Extr. Metall. Rev., (2023) https://doi.org/10.1080/08827508.2022.2073591.
[14] N., Hanilçi, Geological and geochemical evolution of the Bolkardağı bauxite deposits, Karaman, Turkey: Transformation from shale to bauxite. J. Geochem. Explor., (2013), 133, 118-137.
[15] B. Hepvidinli, Investigation of Rare Earth Element Contents of Kızıldağ and Kemiklitepe (Ayrancı-Karaman) Bauxite Mineralizations and Related Source Ores, M.Sc. Thesis, İstanbul Cerrahpaşa University, (2019), İstanbul, Turkey.
[16] T., Uysal, M.E., Akça, H., Sis, M., Erdemoğlu, Optimization of rare earth element recovery from Kızıldağ (Karaman-Türkiye) shale ore using response surface methodology. 18th International Mineral Processing Symposium, (2024), Eskişehir, Türkiye.
[17] T., Uysal, T., Kıyak, H., Sis, M., Erdemoğlu, Effect of intensive milling on the structural characteristics of shale ore. 22nd International Metallurgy and Materials Congress, (2024), İstanbul, Türkiye.
[18] M., Birinci, T., Uysal, M., Erdemoğlu, E., Porgalı, T.S., Barry, Acidic leaching of thermally activated pyrophyllite ore from Pütürge (Malatya-Türkiye) deposit. In: Proceedings of the 17th Balkan mineral processing congress, (2017), Antalya, Türkiye.
[19] P., Pourghahramani, E., Forssberg, Effects of mechanical activation on the reduction behavior of hematite concentrate. Int. J. Miner. Process., 82, (2007), 96-105.
[20] P. Baláž, Mechanochemistry in Nanoscience and Minerals Engineering. Berlin: Springer, (2008), p. 296.
[21] J., Schomburg, Thermal investigation of pyrophyllites, Thermochimica Acta, (1985), 93, 521-4.

BMSM

Bulletin of Materials Science & Metallurgy

Periodical Scientific Journal of UCTEA Chamber of Metallurgical and Materials Engineers

Volume 1, Issue 3, 2024, Pages 7-15 Received: 07 November 2024 Accepted: 25 December 2024

https://doi.org/10.70342/DFDY9265

Research Article

Laser Welding of Aluminum to Copper: Properties of The Welded Joints and Optimization of Parameters

Fatih Şahin[1], Emel Taban[2, *]

[1]Kocaeli University, Dept of Mechanical Engineering, Kocaeli

[2]Welding Research, Education and Training Center, Kocaeli University, Kocaeli

* Corr. Author: emelt@kocaeli.edu.tr

Abstract

Laser welding is a procedure wherein materials are fused together using a beam of high-energy intensity generated through the concentration of light waves. Laser welding has gained significant prominence in the industrial manufacturing sector in recent years due to its various advantages. These advantages include high welding speed, low heat input, narrow weld seams, rapid cooling resulting in minimal heat-affected zones, suitability for automation, successful joining of different materials, and the ability to weld materials of varying thicknesses. In this study, the Taguchi Method was employed to determine the optimal parameters with minimal experimental effort. Mechanical properties, particularly tensile strength, were analyzed using the Minitab software based on the welded joints produced. Detailed examinations were conducted based on predetermined variables for the welding process.

Keywords

Laser welding, dissimilar welding

1. Introduction

Laser welding offers several superior features compared to other traditional welding methods. Due to the low heat input and the formation of a narrow heat-affected zone (HAZ) with laser beams, low residual stresses and distortions occur. Other advantageous aspects include high welding speed, deep penetration capability, flawless weld seams, and high strength values, which are some of the primary advantages provided by laser welding (1). Additionally, high efficiency, cost-effectiveness, and low defect rates are other beneficial characteristics. Dissimilar metal joints are increasingly being applied in various industrial sectors due to their technical and economic advantages. The necessity for hybrid features to meet service conditions is a driving force for the development of new different metal combinations. Copper (Cu) and Aluminum (Al) are among such combinations that need to be developed for applications in electrical connectors, busbars, cooling tubes, heat exchanger tubes, microelectronics, and solar collectors (2). Current efforts toward the electrification of vehicles have significantly increased the demand for a reliable and effective copper welding process (3).

The novelty of this study lies in the investigation of laser welding processes used to join copper and aluminum, specifically focusing on applications in electric vehicle battery configurations, including lithium-titanate-oxide (LTO) and nickel-manganese-cobalt (NMC) cell types. Since vehicles operate under challenging conditions, the quality of the weld and the penetration of materials into each other are critical details. This study further examines the role of the physical properties of the workpiece in determining the quality of the weld seam, particularly the reflectivity, absorption characteristics, and thermal conductivity of the materials (4).

The aim of this study is to identify the challenges encountered in laser welding of copper and aluminum and the methods developed to overcome these challenges. This research fills an important gap in the existing literature by addressing the difficulties arising from differences in material properties, such as reflectivity, high thermal conductivity, thermal expansion, and melting points. The study provides innovative approaches that contribute significantly to the scientific literature, offering solutions to the challenges posed by the dissimilar metal welding of copper and aluminum in laser applications (5).

1.1. Laser Welding Process

The laser welding machine has a single-mode and a maximum power capacity of 1500 watts. The maximum wavelength is 1070 nm. The maximum working area is 200x200 mm. To prevent overheating, it operates integrated with a water-cooled chiller system.

The Taguchi Method was used to find the optimum welding parameters. The welding process was carried out in a wobble pattern. Optimal welding parameters were sought using variables such as beam diameter, frequency, power, and welding speed.

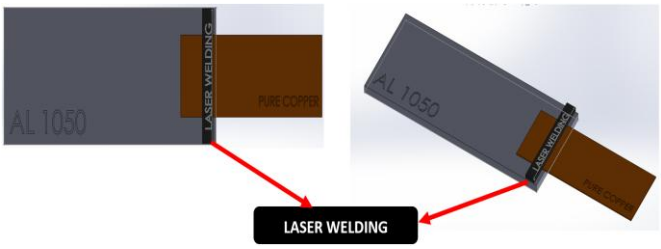

Figure 1. Schematic Representation of the Laser Welding Process [6]

METERIAL	MELTING POİNT (K)	BOILING POİNT (K)	DENSITY ($g.cm^3$)	COEFFICIENT OF LİNEAR THERMAL EXPANSİON X 10^{-6} / (K^{-1})	SPECIFIC HEAT CAPACITY ($J.kg^{-1}.K^{-1}$)	DELASTICITY MODULUS X 10^{-3} (MPa)
COPPER	1356	2573	8.92	16.4	390	108.5
ALUMINIUM	983	2335	2.7	24	880	61.68

Table 1. Properties of Copper and Aluminum Materials [6]

Three different variables were determined as a result of literature research and experiments, and these variables are Laser Power (watt), Welding Speed (mm/s), Amptitude (mm) and Frequency (Hz).

The material selection was inspired by pouch cells, which are critical components in energy storage systems (ESS). In pouch cells, the anode typically consists of 1050 series aluminum, offering high conductivity and corrosion resistance, while the cathode is made of pure copper, known for its excellent electrical conductivity. This configuration is widely utilized in the battery industry to enhance electrical efficiency and minimize energy loss.

In this context, the welding methods employed for joining the cells play a significant role. Particularly in battery systems, the effects of welded joints on mechanical strength, electrical conductivity, and thermal stability are thoroughly analyzed. In this study, the welding process was carried out by overlaying 0.3 mm pure copper material onto 2 mm thick 1050 series aluminum, and this method was investigated in detail. The selected materials and welding parameters were examined within the scope of research aimed at improving efficiency and reliability in battery packaging processes.

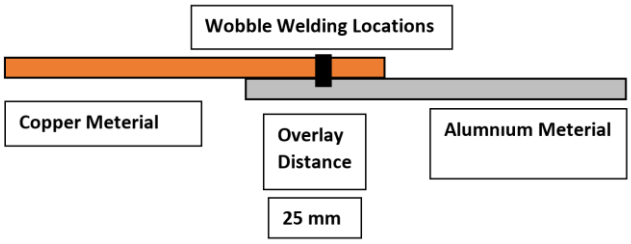

Figure 3. Laser Welding Schematic Representation

Below table shows the L18 experimental design, which includes these four factors (variables) and four different levels. A total of 18 welded joints were made using this design. After research and trials related to these robotic welding joints, the parameters determined within technological limits are shown in Table .. Values corresponding to 1, 2, 3, 4 in each column were placed to create the intended experimental conditions. Based on the tensile strength values of the welded joints made according to the created plan, parameter optimization was performed using Taguchi analysis with the Minitab program. The purpose of using the Taguchi experimental design in this study is to achieve the optimum result with fewer experiments and lower cost, minimizing time loss.

TAGUCCI METHOD EXPERIMENT						
NO	DENEY NO	LASER POWER (W)	WELDING SPEED (mm/s)	AMPTİTUDE (mm)	FREQUENCY (Hz)	HEAT (Kj/mm)
1	T1	1400	120	0,8	140	11,7
2	T2	1400	120	1	150	11,7
3	T3	1400	120	1,2	160	11,7
4	T4	1400	140	0,8	140	10,0
5	T5	1400	140	1	150	10,0
6	T6	1400	140	1,2	160	10,0
7	T7	1400	160	0,8	140	8,8
8	T8	1400	160	1	150	8,8
9	T9	1400	160	1,2	160	8,8
10	T10	1500	120	0,8	140	12,5
11	T11	1500	120	1	150	12,5
12	T12	1500	120	1,2	160	12,5
13	T13	1500	140	0,8	140	10,7
14	T14	1500	140	1	150	10,7
15	T15	1500	140	1,2	160	10,7
16	T16	1500	160	0,8	140	9,4
17	T17	1500	160	1	150	9,4
18	T18	1500	160	1,2	160	9,4

Table 2. Laser Welding Schematic Representation

1.2. Tensile Test Process

The test specimens were extracted from the welded sheets in compliance with the EN 288-4 standard. During the extraction process, visual inspections were meticulously performed to evaluate the weld seam characteristics. As required by the standard, 25 mm sections from the start and end of the welded plates were removed to eliminate potential welding defects in these regions.

The specimens were prepared according to the dimensions specified in the EN ISO 4126:2012 standard and were precisely cut using water jet technology. The cutting process was conducted with a Fagor CNC 8070 L control system, utilizing a water pressure of 4000 bar to prevent thermal distortion in the welded areas and to ensure high precision in the cutting operation.Tensile tests were conducted to evaluate the mechanical performance of the welded joints using an Instron 4411 tensile testing machine. The testing protocol specified a tensile speed of 2 mm/min. Geometric measurements of the specimens were performed with a Mitutoyo caliper featuring an accuracy of 0.01 mm, ensuring high precision in dimensional assessments.

These methodologies facilitated a detailed and reliable analysis of the mechanical and geometric properties of the welded joints. The measurements provided below are expressed in millimeters (mm).

Figure 4. Tensile Testing Sample

1.3. Metallographically Sample Preparation Process

Microscopic analyses were performed to assess the penetration depth and microstructural characteristics of laser-welded joints in detail. Specimens were sectioned from the welded area using a saw operating at 3540 rpm to ensure precise cuts. The extracted samples were then stabilized by embedding them in a cold bakelite mixture prepared by combining 2 parts bakelite powder and 1 part chemical hardener. The mixture was poured over the samples, which were allowed to cure for 15 minutes to achieve a solid and uniform surface.

To prepare the specimens for microscopic evaluation, surface polishing was carried out sequentially using 320, 800, and 1200 grit sandpaper, with each polishing step performed for 1 minute to ensure optimal surface smoothness.

Following the polishing process, the specimens underwent an etching procedure to reveal the microstructural details. Etching solutions were selected based on the material: 3% nitric acid with 97% ethyl alcohol for Aluminum (Al) and 94% ammonium persulfate, 3% iron, and 3% chlorine for Copper (Cu). Specimens were immersed in the etching solution for 15 seconds, after which they were thoroughly rinsed with water to remove any residual chemicals.

In this study, the Axiolab 5 model from ZEISS was used as the electron microscope.Once the preparation steps were completed, the specimens were examined under a digital microscope to analyze the weld penetration depth and microstructural features in detail. This comprehensive analysis process was critical for evaluating the quality and reliability of the laser welding process. This study was conducted using the ZEISS EVO Family SEM. To enable deeper sample analysis, an accelerating voltage of 20 kV was selected. This voltage setting allows for the examination of internal structures with higher resolution, facilitating in-depth analysis of the sample's morphology and composition.

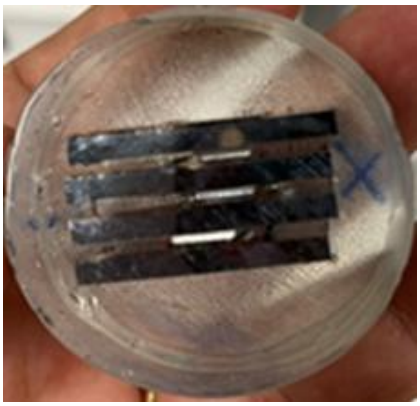

Figure 5. Metallographic Samples

2. Results and Discussion

A total of 54 tensile samples were processed. Three tensile samples were taken for each parameter, and the analyses were conducted based on the sample with the highest value. The following table has been created based on the test results along with the corresponding graphs for the relevant samples.

TAGUCCI METHOD EXPERIMENT						
NO	DENEY NO	HEAT (Kj/mm)	TENSILE FORCE (N) (1)	TENSILE FORCE (N) (2)	TENSILE FORCE (N) (3)	HIGHEST PARAMETER (N)
1	T1	11,7	680,0	1092,0	550,0	1092,0
2	T2	11,7	1012,0	1050,0	1293,0	1293,0
3	T3	11,7	1032,0	650,0	1134,0	1134,0
4	T4	10,0	1024,2	793,3	1038,9	1038,9
5	T5	10,0	1047,0	752,5	572,6	1047,0
6	T6	10,0	615,3	766,2	424,8	766,2
7	T7	8,8	872,2	1159,1	606,4	1159,1
8	T8	8,8	1075,8	1300,0	833,8	1300,0
9	T9	8,8	250,0	383,8	366,8	383,8
10	T10	12,5	400,0	643,5	807,2	807,2
11	T11	12,5	1357,0	705,8	987,9	1357,0
12	T12	12,5	1040,9	1449,7	1037,6	1449,7
13	T13	10,7	907,6	706,8	654,8	907,6
14	T14	10,7	138,8	1022,8	846,7	1022,8
15	T15	10,7	957,7	858,3	1035,6	1035,6
16	T16	9,4	878,7	638,4	1183,9	1183,9
17	T17	9,4	1169,1	917,3	767,2	1169,1
18	T18	9,4	836,2	1026,8	447,4	1026,8

Table 3. Tensile Test Results Table

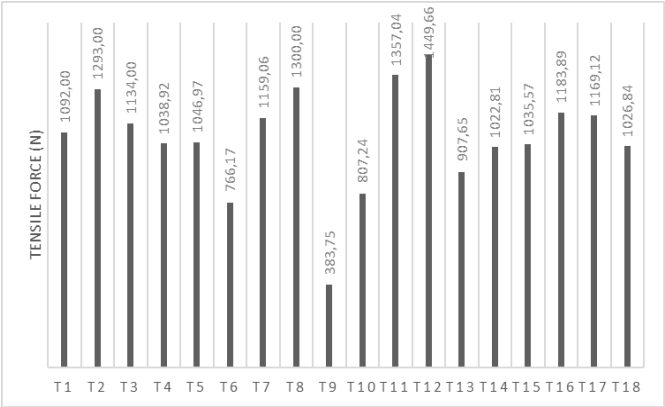

Table 4. Tensile Test Results Table-2

In the tensile test, uniform fractures were observed. It was found that the material fractured in the heat-affected zone (HAZ) of the welded joints. It was observed that the copper and aluminum formed a heterogeneous mixture in the weld pool, which led to fractures at the joint.

Based on the tensile test results, the highest tensile force was used, and analyses were performed using Minitab to determine the optimum welding parameters. The specimens exhibiting the highest tensile strength (T11 and T12), intermediate tensile strength (T2), and the lowest tensile strength (T9) were specifically analyzed. The analysis of the tensile samples reveals the significant impact of the laser welding speed parameter on the welding process. For the first group, the speed parameter was set at 150 mm/s, while for the second group, it was set at 200 mm/s. During the process of adjusting the optimal parameters, the balance between laser power and welding speed is critical. It was observed that as the laser speed increased, the penetration level in the weld area decreased, leading to variations in fracture strength values. An increase in laser welding speed results in faster processing of wobble movements on the weld surface, shortening the duration of laser beam impact. Consequently, the amount of fused metal formed at the weld surface (HAZ) decreased.

According to the tensile test results, it was determined that as the welding speed increased, the penetration decreased, resulting in a decrease in tensile strength values. In the laser welding process, a high laser power and fast welding speed are often preferred. The primary reason for this preference is to prevent overheating by ensuring the welding process on the surface occurs quickly. Additionally, minimal deformations occur in the material. Similarly, the reduction in penetration level has led to a decrease in elongation. As the tensile strength value decreased, the amount of elongation in the material also decreased. The tensile test graph of the T11 specimen, which exhibits high tensile strength, is presented below.

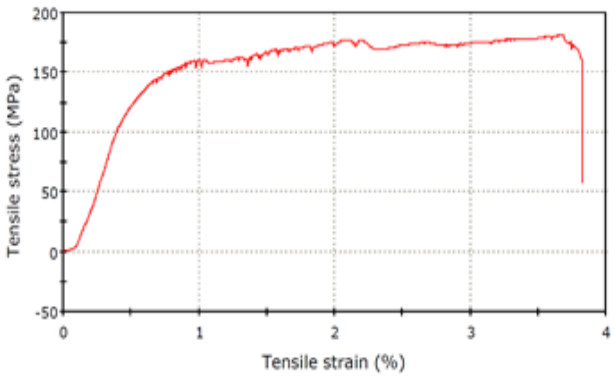

Figure 6. T11 Tensile Test Chart

The T2, T9, T11, and T12 samples identified from the tensile test results were embedded in bakelite. Initially, a 2.5x-50x-200x-500x magnification image was captured from the microscope device to examine the weld penetration area. After etching the samples using an electrolytic etching device, images were taken at 5x magnification, and the penetration distances were measured.

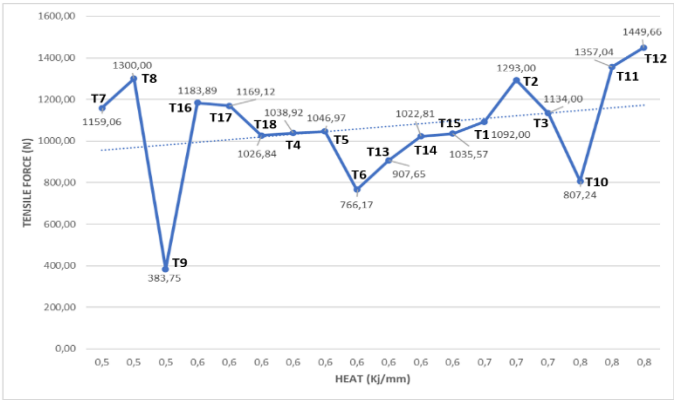

Table 6. Tensile Force and Heat Chart

Based on the obtained data, it was observed that as the penetration amount increased, the strength value of the welded structure also increased. The higher fracture stress in the T11 and T12 samples compared to the other samples supports this observation. In the T9 sample, the fracture stress value was lower than that of the T2 sample, despite having approximately the same penetration distance, due to the presence of an air gap between the two materials.

The analysis of the graph reveals a positive correlation between the heat input and tensile strength. As the heat input increases, it results in a higher amount of material melting and consequently, an increase in penetration depth. The elevation in penetration depth allows for a deeper reach into the material, often leading to the formation of a more robust weld joint. This alignment suggests a parallel relationship between the heat input and tensile strength.

In this context, the escalated heat input enables the propagation of melting and solidification processes into deeper layers of the material, promoting a more homogeneous and sturdy weld structure. Consequently, the molecular bonds between the materials become stronger, thereby enhancing the tensile strength. Thus, the trend depicted in the graph underscores a direct association between the heat input and tensile strength, highlighting the pivotal role of heat input in determining the quality of the weld joint in laser welding processes.

A detailed scanning electron microscopy (SEM) analysis was conducted on the fracture zone, providing valuable insights into the structure of the welded joint. The analysis revealed that the welded joint fractured, separating from its fusion point. This detachment often stems from weak bonds or microstructural disparities at the interface regions, typically arising from the interaction of dissimilar materials. The examination highlighted defects such as gas voids and welding spatters within the weld pool. These imperfections can adversely affect the stability of the welding process and subsequently impact the mechanical properties of the final product. However, it was observed that with the determination of optimal welding parameters and proper control of the welding process, these drawbacks can be minimized. In this context, further experimental studies and parameter optimization are necessary to enhance the quality of the welding process and reduce undesirable defects.

Huang et al. stated the necessity for decreasing the solidification rate to increase tensile strength, which allows for a more homogeneous distribution of solute in the weld pool, complete release of latent heat of solidification, and better matching of crystal lattices. These effects generally indicate the necessity of using an external heat source to increase tensile strength (7).

Stefan and colleagues investigated main parameters such as laser power and welding speed, evaluating their impact on tensile strength. They observed that at low welding speeds, spatters and melt ejections were observed, while higher welding speeds created higher-quality weld seams without visible pores in cross-sections (8).

Tomomichi et al emphasized in their research that decreasing welding speed resulted in increased penetration depth. In this case, while the weld width increased, a deep penetration depth was observed while maintaining a high aspect ratio. This finding suggests that reducing welding speed is one of the factors that increases the material's tensile strength (9).

Ojo and Taban reviews that the tensile strength of laser-welded aluminum alloys is shaped by a combination of microstructure and heat effect. The use of suitable filler metal, optimal welding parameters, and appropriate heat treatment applications can enhance the tensile strength (10).

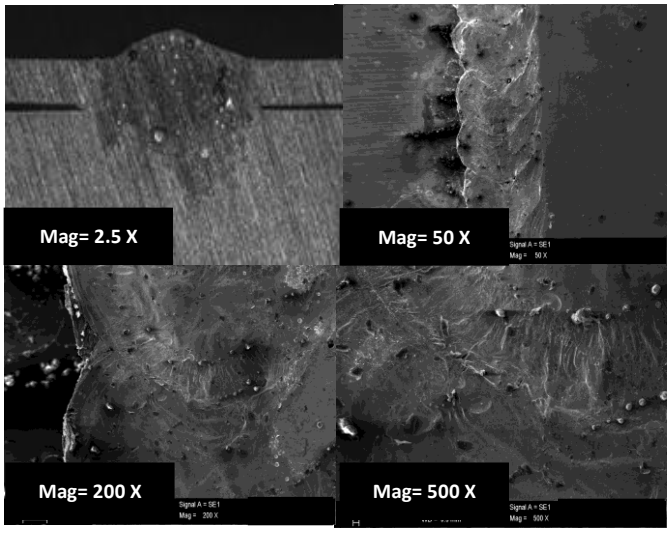

Figure 7. T11 Sample 2.5x-50x-200x-500x Magnified Weld Penetration Zone

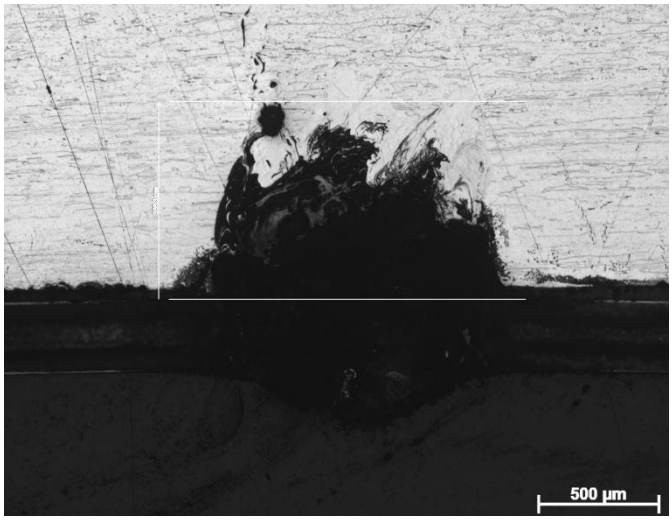

Figure 8. T11 Sample 5x Magnified Weld Penetration Zone

The weld microstructure has a significant impact on tensile strength. The presence of aluminum and copper precipitates in the weld pool and their pinning effect on dislocations can enhance the weld strength (10).

Di Zuo et al predicted in their research that tensile strength would decrease with increasing welding speed. They attributed this to the formation of heterogeneous bond structures and gas voids resulting from the joining of different metals. They argued that welding speed is a significant factor influencing microstructure, fracture behavior, and tensile strength in the process of joining dissimilar metals. Furthermore, regions in the ITAB (Interfacial Transition Active Brazing) zone with copper content ranging from 20% to 50% were found to form a brittle structure, making them more prone to fracture.

It was also noted that increasing the amplitude value increases penetration, thereby positively affecting tensile strength [11].

Trinh et al noted that with the increase in laser power, more metallic material melts and the penetration level increases. This increase leads to the formation of wide and peaked weld seams. They also mentioned that the penetration level increases with the rise in amplitude value. Particularly when high laser power is applied, a noticeable effect on the morphology of the weld seams is observed. Additionally, the effects of laser power on weld morphology were emphasized. As laser power increases, weld spatter and metal melt also increase. However, in welds performed with low laser power, there is a higher likelihood of gas voids forming on the surface. This highlights the importance of correctly adjusting and controlling laser power during the welding process [12].

Hollatz et al have determined that an increase in welding speed results in decreased penetration depth and consequently, a reduction in tensile strength. It was found that an increase in laser power can increase penetration depth while also potentially altering the amplitude value. Moreover, an increase in frequency has been shown to increase penetration, with higher frequencies enabling deeper penetration.

The difference in thermal expansion between materials can lead to the formation of stresses in the solidified material, which may result in cracking. It has been noted that a higher copper content may lead to higher tensile strength, supported by the presence of intermetallic phases. However, a high copper content can also increase the hardness ratio and lead to a more brittle joint, thereby negatively affecting tensile strength [13].

The study conducted by Masoud and his team identified laser power and welding speed as the most critical parameters influencing tensile strength. An increase in laser power generally enhances the maximum tensile strength, whereas an increase in welding speed has the opposite effect, reducing the maximum tensile strength. It was observed that the increase in welding speed reduces the molten base metal area, which adversely impacts the tensile strength [14].

In their study, H. Zhao and colleagues focused on aluminum alloys increasingly utilized in the automotive industry and highlighted the associated challenges and issues. The advantages and disadvantages of laser welding compared to other welding techniques were thoroughly examined. The research reviewed the current understanding of critical physical processes during laser welding of these alloys, including energy absorption in the weld pool, fluid flow, heat transfer, and the evaporation of alloying elements from the weld pool surface.

It was observed that heat-affected zones (HAZ) in laser welding are narrower compared to other fusion welding processes with lower power density, such as gas tungsten arc welding (GTAW) and gas metal arc welding (GMAW). Laser welding of automotive aluminum alloys was tested on tensile specimens, revealing two distinct fracture modes in different regions along the longitudinal direction. Ductile fractures with large surfaces near the fusion zones and in the weld center were observed. Cracks and hot tearing were detected in certain regions following laser welding.Cracking occurring in the weld fusion zone during solidification is identified as solidification cracking, while cracking in the partially melted zone caused by the liquation of low melting point components is termed liquation cracking. In continuous laser welding, 5xxx alloys can be autogenously welded without solidification cracking, whereas 2xxx and 6xxx alloys require the use of filler metals, such as 4043 or 4047, to modify the composition and prevent solidification defects.

Thermal stresses in welds are influenced by the welding process, heat input, joint configuration, rigidity, and the thermal properties of the welded materials. The focal point is critical for weld penetration; as the focal distance increases, penetration depth decreases [15].

Cong and colleagues investigated the effects of oscillation frequency and amplitude on the butt weld formation of 3 mm 6061/2A12 aluminum alloys using the fiber laser welding technique. It was observed that as the oscillation frequency and amplitude increased, the front weld width expanded, while the back weld width gradually decreased. Weld separation, represented by mixing homogeneity, was improved in laser oscillation welding and was primarily dependent on the oscillation frequency, increasing with higher frequencies.

When the oscillation frequency or amplitude was elevated, the mixing intensity of the molten pool increased. The molten pool was accelerated and mixed more uniformly, enabling alloys to be evenly distributed within the weld and detectable near the 6061 base material. The formation mechanism of laser oscillation welding was attributed to the melting of the base material to form a molten pool under laser beam irradiation. Consequently, the beam's oscillation trajectory was critical for the weld morphology.

Laser energy was predominantly concentrated on the upper weld, resulting in an increased front weld width while the back weld width diminished. The results demonstrated that, compared to conventional laser welding, laser oscillation welding significantly improved both the front and back weld morphologies [16].

3. Minitab Analysis And Results

An analysis was performed using the Minitab program based on the fracture stress values from the welded joints. The analysis was conducted according to the previously determined variables for the welding process.

Using the L18 matrix, the parameters were determined, and then the laser welding process was carried out. The analysis of the fracture stress values was performed based on the tensile test results. The effect of a parameter indicates its impact on the determined output. According to the analysis results, the most influential parameter among those used was the welding speed, followed by laser power, amplitude (weld width), and frequency in Table 7.

LEVEL	LASER POWER (W)	VELOCITY (MM/S)	AMPTITUDE (MM)	FREQUANCE (HZ)
1	23,09	24,66	23,38	23,38
2	23,67	23,30	23,38	23,38
3	-	22,19	23,38	23,38
RANK	2	1	3	4

Table 7. Minitab Analysis Outputs

Using the values determined on the L18 matrix, Taguchi's "larger is better" analysis method was employed. The combination of factor values that maximizes the fracture strength of the laser welding was determined with the "Main Effects Plot for Means" graph presented in Table 8.

As seen from the Table 8, increasing the laser power from 1400 watts to 1500 watts has shown a positive effect. Considering the increasing trend in welding speed, a decrease from 120 mm/s to 140 mm/s was observed, while an increase from 140 mm/s to 150 mm/s has shown a positive effect. Increasing the amplitude value from 0.8 mm to 1.0 mm has resulted in a positive effect, but a negative effect was observed between 1.0 mm and 1.2 mm. When the frequency value increased from 140 Hz to 150 Hz, it showed a positive effect, but when it increased from 150 Hz to 160 Hz, it showed a negative effect. Based on the results of this study, optimal parameters have been determined in Table 9.

Fatigue specimens were prepared according to these determined parameters and subjected to fatigue testing. The L18 model was examined based on the fracture stress analyses conducted with the determined parameters, and it was concluded that the model is consistent with a rate of 99.9%. These analyses are depicted in Table 10.

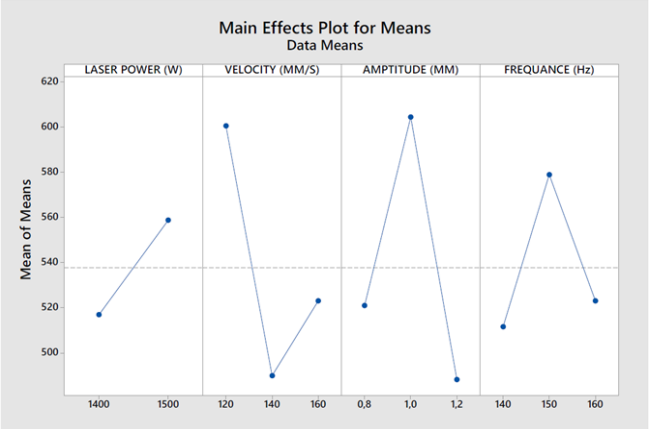

Table 8. Main Effects Plot for Means

KAYNAKLAMA PARAMETRELERİ		OPTİMUM PARAMETRE
A	LASER POWER (W)	1500
B	WELDING SPEED (mm/s)	120
C	AMPTİTUDE (mm)	1,0
D	FREQUENCY (Hz)	150

Table 9. The Optimum Parameter Determined As A Result Of The Analysis

Model Summary

S	R-sq	R-sq(adj)	PRESS	R-sq(pred)
0,0547723	99,90%	99,83%	0,0972	99,67%

Table 10. Percent Accuracy Of Experiment

This study investigated the effects of laser welding on important factors such as tensile strength, microstructure, heat input, and IMC (Intermetallic Compound) thickness. Our findings revealed that an increase in welding speed led to decreased penetration depth and consequently, reduced tensile strength. Similarly, while an increase in laser power increased penetration depth, an increase in frequency resulted in increased penetration, with higher frequencies enabling deeper penetration.

The difference in thermal expansion between materials was found to induce stresses in the solidified material, potentially leading to crack formation. It was observed that a higher copper content could lead to higher tensile strength, but also to a more brittle joint, negatively impacting tensile strength. These findings underscore the importance of laser welding in the material joining process.

4. Conclusions

This study systematically examined the impact of laser welding parameters on the joining of Aluminum (Al) and Copper (Cu) materials, with a focus on key performance indicators such as tensile strength, microstructural integrity, heat input, and intermetallic compound (IMC) layer thickness. The results clearly indicate that laser welding parameters play a pivotal role in determining the quality and mechanical properties of welded joints.

The experimental findings established that increasing welding speed reduced penetration depth, thereby negatively influencing tensile strength. Conversely, higher laser power enhanced penetration depth, contributing positively to joint performance. Variations in frequency were observed to significantly affect penetration depth, with higher frequencies achieving greater penetration but introducing increased thermal stress.

The interaction within the weld pool revealed a heterogeneous mixture of Al and Cu, which influenced the formation of the heat-affected zone (HAZ) and the fracture behavior of the joints. It was determined that differential thermal expansion between the materials induced residual stresses during solidification, potentially leading to crack formation. Additionally, a higher copper content improved tensile strength but increased brittleness, adversely impacting overall mechanical performance.

To identify the optimal welding conditions, the Taguchi method was applied, and parameters were optimized. Fatigue tests conducted with the identified parameters demonstrated the reliability of the optimization process, yielding a model accuracy of 99.9%. These outcomes highlight the effectiveness of the employed methodology and underscore the critical importance of precise parameter control in laser welding processes.

In summary, laser welding has been validated as a highly effective technique for joining dissimilar materials with distinct physical and chemical properties. However, the necessity for meticulous parameter optimization to ensure weld quality and performance cannot be overstated. The insights derived from this study provide a robust foundation for the application of laser welding in high-stakes industries such as battery manufacturing, while also contributing to the advancement of state-of-the-art material joining technologies.

Authors' Contributions

Conceptualization, methodology, investigation, data curation, and writing original draft preparation: Fatih Şahin. Supervision and project administration: Prof. Dr. Emel Taban.

Declaration of Competing Interest

The authors declare that they have no known competing financial interests or personal relationships that could have appeared to influence the work reported in this paper.

References

[1] Florian Fetzer, Michael Jarwitz, Peter Stritt, Rudolf Weber, Thomas Graf, Fine-tuned Remote Laser Welding of Aluminum to Copper with Local Beam Oscillation, Physics Procedia, Volume 83, 2016, Pages 455-462.

[2] Mehta KP, Badheka VJ. A review on dissimilar friction stir welding of copper to aluminum: process, properties and variants. Material and Manufacturing Processes; 2015.

[3] R.S. Chopde, S.P. Gadewar, Optimization of laser welding parameters for Copper and aluminum joint, International Engineering Research Journal Page No 21-28.

[4] Recep Uzun, Ömer Keleş, 2012, Examination of the effects of welding parameters on welding quality in laser welding process, Journal of Faculty of Engineering and Architecture, Gazi University.

[5] Matteo Garavaglia, Ali Gökhan Demir, Stefano Zarini, Brian M. Victor, Barbara Previtali. (2019) Process development and coaxial sensing in fiber laser welding of 5754 Al-alloy. Journal of Laser Applications 31:2, 022419.

[6] Huang, J. , Shi, W. , Xie, Y. , Liang, Z. and Zhan, J. (2019) Analysis of Laser Micro Welding of Copper-Aluminum Dissimilar Metals and Its Mechanism. Journal of Applied Mathematics and Physics, 7, 3192-3200

[7] Huang, J. , Shi, W. , Xie, Y. , Liang, Z. and Zhan, J. (2019),Analysis of Laser Micro Welding of Copper-Aluminum Dissimilar Metals and Its Mechanism. Journal of Applied Mathematics and Physics, 7, 3192-3200. https://doi:10.4236/jamp.2019.712224.

[8] S. Liebl, R. Wiedenmann, A. Ganser, P. Schmitz, M.F. Zaeh,Laser Welding of Copper Using Multi Mode Fiber Lasers at Near Infrared Wavelength,Physics Procedia,Volume 56,2014,Pages 591-600,ISSN 1875-3892, https://doi.org/10.1016/j.phpro.2014.08.047.

[9] Tomomichi Yasuoka*, Takashi Kayahara*, Ryosuke Nishii*, Keigo Matsunaga*, Takashi Shigematsu,Welding With the High Beam Quality Fiber Laser and Suppression of Welding Defects Using the Beam Mode Control Technology,Furukawa Electric Review, No. 50 2019

[10] Ojo, O.O., Taban, E. Trend and innovations in laser beam welding of wrought aluminum alloys. Weld World 60, 415–457 (2016). https://doi.org/10.1007/s40194-016-0317-9

[11] Di Zuo, Shengsun Hu, Junqi Shen, Zhiqing Xue, (2014),Intermediate layer characterization and fracture behavior of laser-welded copper/aluminum metal

joints,Materials & Design, https://doi.org/10.1016/j.matdes.2014.02.004.

[12] Trinh, L.N.; Lee, D. The Characteristics of Laser Welding of a Thin Aluminum Tab and Steel Battery Case for Lithium-Ion Battery. Metals 2020, 10, 842. https://doi.org/10.3390/met10060842

[13] Hollatz, S., Heinen, P., Limpert, E. et al. Overlap joining of aluminium and copper using laser micro welding with spatial power modulation.Weld World 64, 513–522 (2020). https://doi.org/10.1007/s40194-020-00848-9

[14] Masoud Harooni, B. C. (2013). Effect Of Process Parameters On The Weld Quality İn Laser Welding Of AZ31B Magnesium Alloy in Lap Joint Configuration. In International Congress on Applications of Lasers & Electro-Optics (Vol. 20), s. (https://doi.org/10.2351/1.5062923).

[15] H. Zhao, D. W. (1999). Current İssues And Problems İn Laser Welding Of Automotive Aluminium Alloys. International Materials Reviews, 44:6, 238-266,, s. (https://doi.org/10.1179/095066099101528298).

[16] Cong Chen, Y. X. (2020). Weld Formation Mechanism Of Fiber Laser Oscillating Welding Of Dissimilar Aluminum Alloys. Journal of Manufacturing Processes, 60, 180-187, s. (https://doi.org/10.1016/j.jmapro.2020.10.050).

BMSM

Bulletin of Materials Science & Metallurgy

Periodical Scientific Journal of UCTEA Chamber of Metallurgical and Materials Engineers

Volume 1, Issue 3, 2024, Pages 16-19 Received: 06 December 2024 Accepted: 25 December 2024

https://doi.org/10.70342/UKTF5630

Research Article

Investigation of the Effect of Thermo-Mechanical Processing Orientation on the Final Material Performance in 6xxx Aluminium Alloys Produced With High Recycling Rates

Zeynep Tutku Ozen[a]*, Irem Yaren Siyah[a], Ilyas Artunc Sari[a], Melih Caylak[a], Gorkem Ozcelik[a], Burak Kardesler[a], Ibrahim Bat[a]

[a] ASAS Aluminyum A.S., Turkiye

*Corresponding author's email: tutku.ozen@asastr.com

Abstract

Recycling of aluminium alloys is crucial due to its effects on environment, economy and social situations. It is also a popular research topic for aluminium producers and aluminium end users like automotive industry due to its tremendous effects on final carbon equivalent value and price. This scientific study emphasizes the critical importance of recycling in alloys used in the automotive sector, investigating the effects of thermo-mechanical processing orientation on the final material performance of 6XXX aluminium alloys with high recycling rates. Specifically, materials obtained using high recycling rates on 6063 and 6082 alloys produced for the automotive industry have been examined. The study aims to evaluate the mechanical properties of materials under thermal load through methods such as anisotropic strength correlations and bake-paint testing. The central focus of the study is to establish correlations between mechanical properties in different orientations based on thermal inputs. Data obtained through mechanical tests and bake paint tests conducted at 0, 45, and 90-degree orientations to extrusion direction play a crucial role in determining the material's performance. The findings contribute to our understanding of the impact of 6XXX aluminium alloys produced with high recycling rates on the final material performance in industrial applications.

Keywords

Recycling; Anisotropy; Aluminium Alloys, Thermo-Mechanical Properties

1. Introduction

Recycling of aluminium alloys has great importance due to its environmental, economic, and social impacts. Recycling conserves natural resources, saves energy, and lowers the carbon footprint. Consequently, advancing and implementing recycling techniques is a vital research focus for aluminium alloy producers and end users [1].

The automotive industry is one of the biggest industries that is in the use of recycled aluminium alloys due to its demand for lightweight and strong materials with low carbon footprint amounts. This demand both increases the performance of vehicles and provides environmental benefits by improving fuel efficiency. 6XXX series aluminium alloys, especially 6063 and 6082 aluminium alloys, are widely used in automotive applications due to their excellent mechanical properties and corrosion resistance [2]. However, studies are continuing to examine the effects of these alloys produced with high recycling rates on the final material performance [3].

Aluminium alloys produced with increased recycling content may not exhibit the same properties as alloys produced with primary contents even their similar nominal chemical compositions. This discrepancy arises from the mixing of scraps, the potential presence of impurity elements, and residual oxide inclusions. These inclusions can form intermetallic phases of varying nature, whose size, morphology, and distribution can significantly influence the alloy's physical and mechanical properties [4].

According to relevant studies such as [4,5], it can be noticed that recycling content increase both harm and benefit the final properties of the aluminium alloys. Bruschi et al. have studied machinability and mechanical properties of recycled and primary aluminium alloys. They have find that, increased recycling content may cause ductility decrease due to Fe-rich

intermetallic [4]. Ouyang et al. have studied enhancing joining mechanical properties. They have come up with following correct strategy to recycle waste sheets to enhance the joining mechanical properties of aluminium alloys experimentally proven to be useful. In addition, it has the effect of reducing the joint bulge height and improving joint aesthetics [5].

This study aims to investigate the effects of 6XXX series aluminium alloys produced with high recycling rates on the final material performance depending on the thermo-mechanical processing orientation. Mainly, this research on 6063 and 6082 aluminium alloys produced for the automotive industry uses methods such as anisotropic strength correlations and bake-paint tests to evaluate the mechanical properties of the materials under thermal load.

Anisotropy behavior of the alloys are investigated to get an idea over the thermo-mechanical process effects with respect to process direction of the profiles. Different specimens are prepared and subjected to tensile testing with perpendicular, diagonal and parallel directions to extrusion. Bake-Paint test is performed to determine the changes in mechanical properties of parts produced in the automotive industry after post-painting process [6].

Mechanical tests and bake-paint tests at different orientations (0, 45, and 90 degrees) to determine the performance of the material are conducted.

In this study effects on the final material performance of 6XXX series aluminium alloys produced with high recycling rates in industrial applications depend on the thermo-mechanical processing orientation have been discussed. The results obtained aim to increase the use potential of recycled aluminium alloys in various industrial applications, especially in the automotive sector.

2. Materials and Methods

In this paper, the experimental procedures illustrated on Figure 1 have been applied to investigate the effects of temperature and orientation effects on high recycling ratio 6063 and 6082 alloys. After profile production, tensile tests and bake paint tests have been applied to the samples.

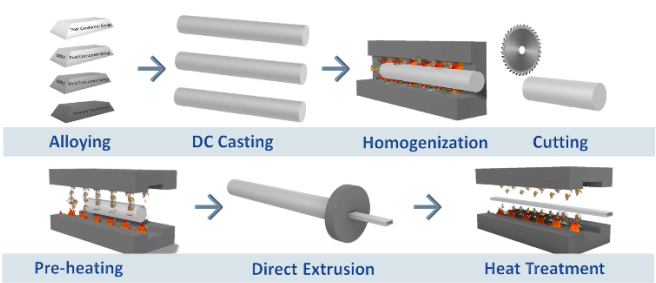

Figure 1. Experimental setup for analyzing high recycling ratio aluminium alloys.

2.1. Materials

To begin with the protype profile production with 6082 and 6063 alloys ASAS's prototype casting facility has been used with 500 kg capacity. Used materials ratios have been showed at Table 1.

Table 1. Composition of raw materials used in as-cast alloy production.

	6063	**6082**
Post-Consumer Scrap	16%	34%
6063 Post Consumer Scrap	54%	12%
6063 Post Consumer Scrap	-	44%
Primary Feedstock	30%	10%

After casting 14 inches extrusion billets they have been investigated by optical emission spectroscopy (OES) analysis to validate alloy composition according to the TS-EN 573-3 [7] chemical composition standard. Table 2 demonstrates the OES results after casting.

Table 2. OES results for the chemical composition of as-cast 6XXX alloys.

	Content wt. %						
	Si	**Fe**	**Cu**	**Mn**	**Mg**	**Cr**	**Zn**
6063	0,55	0,23	0,02	0,06	0,55	0,01	0,05
6082	0,88	0,25	0,75	0,62	0,86	0,06	0

Casted billets have been tested by ultrasonic control in order to determine their suitability for extrusion with respect to ASTM 594-9 Class A [8]. Acceptable billets have been homogenized in ASAS's homogenization furnace. 6063 alloys have been homogenized by heating up to 570°C for 6 hours and keeping at 570°C for 6 hours. 6082 alloys have been homogenized by heating up to 555°C for 6 hours and keeping at 555°C for 6 hours. Homogenized billets have been extruded at ASAS's 62 MN extrusion press which is the biggest extrusion press in Turkey. 6063 billets have been extruded with 556°C exit temperature and 7,5 mm/s speed. 6082 billets have been extruded with 533°C exit temperature and 5,1 mm/s speed.

Extruded profiles have been cut to the length to get $A30_{mm}$ tensile test specimens. In order to carry out anisotropy analysis specimens that are parallel to extrusion direction (0°), specimens that are diagonal to the extrusion direction (45°) and specimens that are perpendicular to the extrusion direction (90°) have been prepared. Both anisotropy and bake paint tensile tests are carried out at 250 kN Zwick Tensile Testing Device with respect to EN ISO 6892-1:2020 [9] standard. Bake paint tests are applied to the specimens after exposing them to 180°C for 20 minutes.

3. Results and Discussion

In the analysis of anisotropy and bake paint tests, 5 samples have been tested. Their average values and standard deviations are stated as results. Anisotropy analysis results have been showed at the Table 3.

Table 3. Anisotropy analysis results at different orientations.

	Angle	Rp0,2 [MPa]	σ	Rm [MPa]	σ	A (%)	σ
6063	0°	244	4,4	270	4,3	13,6	4,1
	45°	238	4,2	257	4	9,66	4,1
	90°	222	3,4	258	3,2	11,23	3,3
6082	0°	267	4,3	293	4,1	15,3	4
	45°	264	2,7	287	2,6	9,1	2,8
	90°	276	2,4	300	2,4	9,25	2,3

According to the results yield strengths of 6063 alloys decrease from parallel to perpendicular direction. While yield strength of the 6082 alloys increases from the direction of 0° to 90° while it shows lowest value at 45°.

Tensile strength of the alloys showed similar behavior with yield strengths. When the testing direction is diagonal and perpendicular to the extrusion direction, tensile strengths of the 6063 alloys 4-5% lower than the 0°. This behavior is primarily due to the alignment of grains and precipitates along the extrusion direction. Highest tensile strength values are achieved with testing in 0° angle for 6063 alloys. 6082 alloys highest strength seen at 90° angle. The tensile strength of this alloys has decreased from 0° to 45°. The unexpected result of 6082 alloy can be explained by its high alloying rates and Cu elements has created Al_2Cu precipitates which caused directional strengthening [10].

Elongation percentage of the alloys have the highest ratios comparing the other directions for both alloys at 0°. In the 45° specimen for 6063 alloy, elongation decreased more than 30% comparing to 0°. The sharp decrease in elongation at 45° for 6063 alloy is attributed to the anisotropic distribution of second-phase particles, which act as stress concentrators and reduce plasticity. In the case of 6082 alloy, elongation values of 45° and 90° are very similar, reflecting a more uniform distribution of strengthening phases.

From the results of anisotropy analyses it can be discussed that, aluminium extrusion alloys should be designed with respect to their expected properties and extrusion directions should be arranged upon this theory. When high strength is crucial for final applications, 90° results are better for 6082 alloy while 0° better for 6063 alloy. When high elongation is important for final application, 0° results are better. According to this knowledge one can select or design aluminium extrusion profiles with respect to end users' criteria.

Table 4. Bake-paint test results for mechanical properties.

	Rp0,2 [MPa]	σ	Rm [MPa]	σ	A (%)	σ
6063	258	3,1	274	3	12,2	3,2
6082	279	2,9	306	2,9	15	3,1

According to bake paint results it can be noticed that yield and tensile strength of both 6063 and 6082 alloys have been increased. However, elongations of both alloys have been slightly decreased. This process promotes the formation of fine, coherent precipitates (e.g., Mg_2Si in 6063 and Al_2Cu in 6082), which impede dislocation motion and enhance strength. The more significant increase in 6082 alloy can be attributed to its higher alloying content, which provides a greater potential for precipitation strengthening. The decrease in elongation after the bake-paint test is a typical consequence of increased precipitation density. While the precipitates improve strength, they also reduce the material's ability to deform plastically, leading to lower elongation. According to these results it can be discussed that the thermal treatment applied before tensile test section of bake paint test has increased the strength of the alloys. As characteristics of aluminium alloys, one can notice that, these alloys have converged to the peak age aging condition.

4. Conclusion

This study demonstrates the critical influence of thermo-mechanical processing orientation on the performance of 6XXX series aluminium alloys with high recycling rates, particularly in automotive applications. The anisotropy analysis revealed that mechanical properties such as yield strength, tensile strength, and elongation vary significantly with orientation. For 6063 alloy, the highest yield and tensile strength were observed along the extrusion direction (0°), whereas the 6082 alloy exhibited superior properties at the perpendicular direction (90°). These variations are excepted to be caused from distinct alloying elements and their influence on precipitation behavior, particularly the formation of Al_2Cu precipitates in 6082 alloy.

The bake-paint tests confirmed a notable increase in yield and tensile strength post-thermal treatment, accompanied by a slight reduction in elongation. This is consistent with the alloys reaching peak age-hardening conditions. Yield strength increased by approximately 6% for both alloys after bake-paint testing. Tensile strength changes ranged between 4% and 7%, depending on the orientation and alloy type. Elongation decreased by 10%-15% after thermal treatment.

As a conclusion, material properties are highly related to their designs and processing. For automotive end users, 6082 alloys can be selected for high strength requirements such as battery box. However, 6063 alloy can be selected for moderate strength and elongation requirements. As engineering is highly

related to optimization, investigating anisotropy behaviour of the metals serves best for this approach.

Authors' Contributions

Conceptualization: Zeynep Tutku Ozen, İrem Yaren Siyah, İbrahim Bat; Methodology: Zeynep Tutku Ozen, İlyas Artunç Sarı, Burak Kardeşler, Melih Çaylak; Investigation: İrem Yaren Siyah, Zeynep Tutku Özen, İbrahim Bat, İlyas Artunç Sarı, Burak Kardeşler, Melih Çaylak; Validation: Zeynep Tutku Özen, Görkem Özçelik, İrem Yaren Siyah, İlyas Artunç Sarı, İbrahim Bat, Burak Kardeşler; Writing—original draft preparation: Zeynep Tutku Özen, İrem Yaren Siyah, İlyas Artunç Sarı; Writing—review and editing: Zeynep Tutku Özen, İrem Yaren Siyah, İlyas Artunç Sarı; Supervision: Zeynep Tutku Özen, Görkem Özçelik.

Declaration of Competing Interest

The authors declare that they have no known competing financial interests or personal relationships that could have appeared to influence the work reported in this paper.

Acknowledgement

This paper has been studied in a Horizon 2020 project called SALEMA with grant agreement number of 101003785. ASAS Aluminyum R&D department and SALEMA project partners are acknowledged due to their high effort and great contributions.

References

[1] Z. T. Ozen et all, Enhancing Recycling Efficiency and Critical Raw Material Substitution in 6xxx Alloys Production with Respect to Their Extrusion Feasibility and Mechanical Properties, TMS, (2024)

[2] Halme, Kimmo & Piirainen, Kalle & Vekinis, Georgios & Sievers, Udo & Viljamaa, Kimmo. (2012). Substitutionability of Critical Raw Materials. 104

[3] Billy, R. G., & Müller, D. B. (2023). Aluminium use in passenger cars poses systemic challenges for recycling and GHG emissions. Resources, Conservation and Recycling, 190, 106827. https://doi.org/10.1016/j.resconrec.2022.106827

[4] Bruschi, S., Bertolini, R., Ghiotti, A., Mahmood, H., & Zanella, C. (2024). Machinability of Recycled Aluminum Alloys. Manufacturing Letters, 41, 1669–1675. https://doi.org/10.1016/j.mfglet.2024.09.194

[5] Ouyang, X., Zhang, H., & Chen, C. (2023). Recycling of scrap sheet material: Enhanced joining mechanical properties of aluminum alloys by a novel auxiliary sheet flat-clinching process. Journal of Materials Research and Technology, 25, 4609–4621. https://doi.org/10.1016/j.jmrt.2023.06.209

[6] Orji, C., Lombardi, A., Benkel, F., Birsan, G., Byczynski, G., Sadayappan, K., Hamed, M., & Shankar, S. (2023). The Paint Bake Intervention: The effect of paint bake treatment on Al-Fe (zn, mg) alloy castings for structural automotive application. Proceedings of the 62nd Conference of Metallurgists, COM 2023, 351–356. https://doi.org/10.1007/978-3-031-38141-6_41

[7] Turkish Standards, European Norm [TS-EN]. (2024). Aluminium and aluminium alloys - Chemical composition and form of wrought products - Part 3: Chemical composition and form of products (TS-EN 573-3)

[8] American Society for Testing and Materials. (2021). Standard Practice for Ultrasonic Inspection of Aluminum-Alloy Wrought Products (ASTM B594)

[9] European Norm, International Organization for Standardization. (2020). Metallic materials - Tensile testing (EN-ISO 6892-1: 2020)

[10] Bonatti, R. S., Rodrigues, J. F., Peixoto, L. C., Baldo, R. F., Bortolozo, A. D., & Osório, W. R. (2023). Anisotropic tensile and compressive strengths of al-4WT.%Cu alloy powder: Part 2- effect of dendritic arm spacings. Metals, 13(7), 1282. https://doi.org/10.3390/met13071282

BMSM

Bulletin of Materials Science & Metallurgy

Periodical Scientific Journal of UCTEA Chamber of Metallurgical and Materials Engineers

Volume 1, Issue 3, 2024, Pages: 20-24 Received: 07 November 2024 Accepted: 26 December 2024

https://doi.org/10.70342/LCHL4063

Research Article

Effects of Alkali Ratios on Alkali Barium Glasses for Compression Sealing

Tutku Turgutlugil Gökçe [a, b]*, M. Kaan Pehlivanoğlu[a], N. Kaan Çalışkan[a] and Abdullah Öztürk[b]

[a]Fundamental Materials Technologies Application Division, TÜBİTAK- SAGE

[b] Metallurgical and Materials Engineering, Middle East Technical University

*Corresponding author's email: tutku.turgutlugil@tubitak.gov.tr

Abstract

Alkali barium glasses of the system SiO_2, Al_2O_3, LiO_2, K_2O, Na_2O, and BaO were produced using high-purity powders by the melt-quench technique to evaluate the suitability of these glasses for hermetic sealing. Six different glasses with varying Na_2O and K_2O content were produced. Although both Na and K are alkali elements, their different ionic radii and densities result in different effects on the glass network structure. As a result, they have caused changes in the properties of the glass, leading to alterations in the glass-metal interface as well. Although the total Na_2O + K_2O content of the glasses was maintained at 15 wt%, the Na_2O/K_2O ratio was varied to see the effect of compositional variation on the properties of the glasses produced. In this study, it was observed that as the Na_2O/K_2O ratio increases, properties such as density, Tg, and chemical durability of the alkali barium glass decrease, while CTE increases. Glass pellets, prepared from the glass powders, were used for sealing with 304 stainless steels at different sealing profiles under argon gas. The results revealed that the sealing profile and the alkali ratios (Na_2O/K_2O) of the glass have a profound effect in the microstructure and the interface characteristics of the compression sealing developed between the alkali barium glass and 304 stainless steels.

Keywords

Alkali Barium Glass, Hermetic, Compressive Sealing

1. Introduction

Glass-to-metal (GTM) seals have played critical roles in hermetic packaging technologies for over fifty years. Among the various hermetic sealing methods, compression sealing, characterized by metallic holders with higher coefficient of thermal expansion (CTE) than glasses, stands out [1,2]. For a common example of compression sealings, 304 stainless steel (304 SS) as metallic holder with a CTE of 17.8 x 10-6/°C [3] is sealed with alkali barium glasses (e.g., Corning 9013) exhibiting CTE values in the range of 8.8-9.3 x 10^{-6}/°C, and Alloy 52® as pin material with a CTE of 9.5-9.8 x 10^{-6}/°C. This sealing imparts enhanced strength through compression [4]. One of the common categorizations of sealing glass is "Soft" and "Hard" glasses. Soft glass seals utilize glasses with a working range of approximately 1000 °C and a CTE in the order of 9 x 10-6/ °C [1,3,5].

For effective glass seals, the glass must exhibit wetting behaviour on the metallic holder, creating adhesion between the materials [6,7]. Beyond the sealing profile, effective glasses for GTM sealing must possess key properties, including thermal expansion compatibility with metal components, good adhesion on metal pieces, high chemical durability [8,9]. Another important parameter for a good sealing with strong bonds, either chemically or mechanically are glass composition and sealing treatment [10].

This study aims to optimize the sealing properties of alkali barium glasses, specifically enhancing the CTE, Tg, density, and sealing interface characteristics, while also improving their chemical durability. Glasses with varying Na_2O/K_2O ratios were produced, and the effects of these ratios on the properties of alkali barium glasses, as well as the differences in the glass-metal adhesion interfaces, were investigated. In particular, the influence of the Na_2O/K_2O ratio on the properties of the glasses was thoroughly examined, revealing the structural-property relationship in these glasses.

2. Materials and Methods

The glasses were produced using the melt-quench technique, which offers several benefits, including the production of homogeneous glass with reduced internal stresses, resulting in stronger and more durable materials. Additionally, this method allows for the production of different compositions, easily. Alkali barium glasses, produced with SiO_2, Al_2O_3 LiO_2, K_2O, Na_2O and BaO. SiO_2 and Al_2O_3 were used in their pure powder forms other powders were sourced from lithium carbonate (Li_2CO_3), potassium hydroxide (KOH), sodium hydroxide (NaOH), and barium carbonate ($BaCO_3$) powders, respectively.

The powders were meticulously mixed and subjected to melting at 1550 °C for 30 min in a platinum crucible under ambient conditions. Quenching of the molten glass was achieved by dipping the bottom of the platinum crucible into a container filled with water. To ensure the homogeneity of the glass, this melting process was repeated three times. Following the third melting cycle, the molten glass was cast into a molybdenum mold. The glass compositions produced are presented in Table 1.

Table 1. Compositions of the glasses produced.

Glasses	Composition (wt%)					
	SiO_2	Al_2O_3	Li_2O	BaO	Na_2O	K_2O
A-1	65	5	3	12	3	12
A-2	65	5	3	12	6	9
A-3	65	5	3	12	9	6
A-4	65	5	3	12	12	3
A-5	65	5	3	12	15	-
A-6	65	5	3	12	-	15

For the sealing treatments, glass pellets were prepared with glass powders which were obtained from third melting procedure of glass. Following crushing, the glass powders were sieved to particle size less than 25 µm. The next step involved the dry pressing of the glass powders utilizing a uniaxial hydraulic press operating at 38 MPa. This method was employed to compact the glass powders efficiently.

To verify the amorphous nature of the samples, XRD analysis was systematically conducted on all specimens using Rigaku-Miniflex 600 X-ray diffraction analyzer. Compositional analysis of all glasses was obtained using an Energy-Dispersive X-ray Spectroscopy (EDS) system integrated with a Scanning Electron Microscope (SEM) using the Hitachi-FlexSem instrument. The density of the glasses was determined using Archimedes' technique. CTE for the glasses was determined utilizing the Linseis-L75 Vertical Bench Top Model dilatometer. Measurements were conducted over the temperature range of 25 to 500 °C with a controlled heating rate of 4 °C/min. Before the measurements, all glasses were annealed, at 600 °C for 1 h.

A-4 glass was selected for sealing treatments. Sealing profile was carried out first at temperatures of 920, 950, and 980 °C than at second temperatures of 450 and 480 °C. The holding period at the first temperature was 20 min, while it was 1 h at the second temperature. The heating and cooling rates were maintained at 5 °C/min. The examination of the sealing interface between glass and metal was conducted through SEM under high vacuum conditions.

3. Results and Discussion

The XRD patterns for all the glasses (A-1, A-2, A-3, A-4, A-5, and A-6) exhibited no crystalline peaks as shown in Figure 1. No matches with crystalline peaks were evident in the XRD software analysis, confirming their amorphous nature.

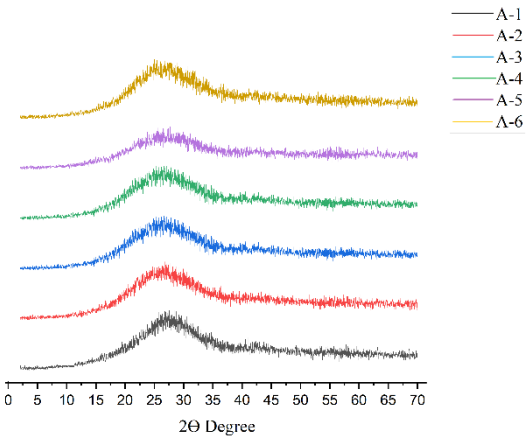

Figure 1. XRD patterns for all glasses.

Chemical composition as determined by EDS for all glasses are presented in Table 2. According to the EDS results, Na_2O and K_2O contents are nearly the same with intended compositions. However, SiO_2 and BaO contents can show different results from intended compositions. This is attributed to incapability of EDS in detecting Li_2O.

Table 2. EDS results for all glasses.

Glasses	Composition (wt%)				
	SiO_2	Al_2O_3	BaO	Na_2O	K_2O
A-1	65.30	6.32	12.29	2.57	11.52
A-2	64.53	7.62	13.41	6.60	7.94
A-3	64.34	7.79	14.18	8.60	5.09
A-4	63.93	6.96	13.77	12.30	3.04
A-5	66.68	6.90	11.30	14.93	-
A-6	69.85	6.94	11.12	-	13.08

The variation of CTE with temperature for all glasses are shown in Figure 2. Two critical results obtained from this CTE values. First one is CTE values exhibit an increasing trend with rising temperature, emphasizing the crucial role of temperature in influencing CTE of glass [11,12]. The second one is that CTE varies with composition. An increase in Na_2O content led to higher CTE values.

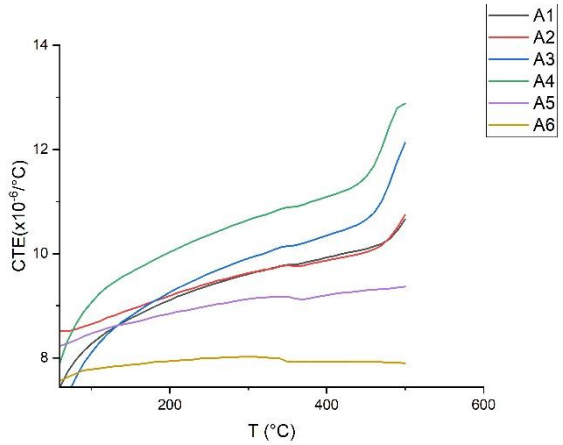

Figure 2. CTE results graphs for all glasses.

In sealing experiments, A-4 was selected as the test sample across all sealing profiles. This choice was motivated by two primary factors. Firstly, A-4 illustrated the lowest Tg, it was more affected by the second sealing temperature than the other glasses. Secondly, with the highest CTE, A-4 demonstrates superior spreading on surfaces, providing a clear illustration of the bonds between glass and metal.

3.1 Sealing Results for A-4 Glass

The images taken from a sealing profile for A-4 glass and 304 SS at temperatures of 920 and 450 °C is shown in Figure 3. In Figure 3 clear interface is observed between GTM. EDS line (yellow line) indicates the region analysed for elemental composition. EDS reveals dendritic Fe structures inside the glass. Dendritic Fe structures contribute to strong mechanical bonds, also the Fe ion saturated the glass gives strong chemical bonds between GTM [12].

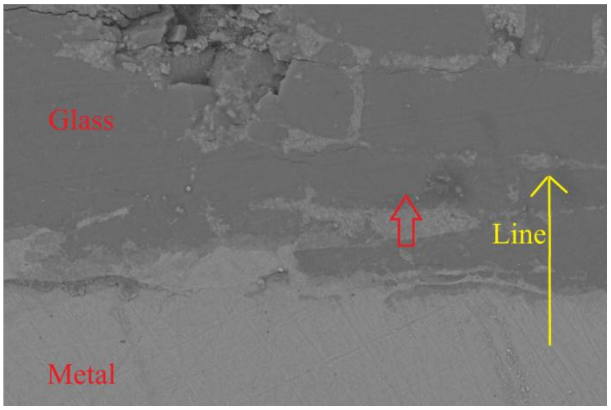

Figure 3. GTM interface for A-4 glass with a sealing profile at temperatures of 920 and 450 °C at X5000.

The second sealing profile for A-4 is at temperatures of 920 and 480 °C. When it is examined, it is clearly observed that, interface is not saturated with Fe ions. This can be as a result of weak Van der Waals bonds. The presence of cracks in glass may be due to differences in CTE between 304 SS and glass.

Figure 4 depicts the sealing interface for A-4 at the sealing profile at temperatures of 950 and 450 °C. Figure 4 shows the bonds between glass and metal, resembling a dendritic structure. EDS analysis detects these Fe ions, which appear dendritic inside the glass. The saturation of the glass with Fe ions suggests the presence of strong chemical bonds between them [12].

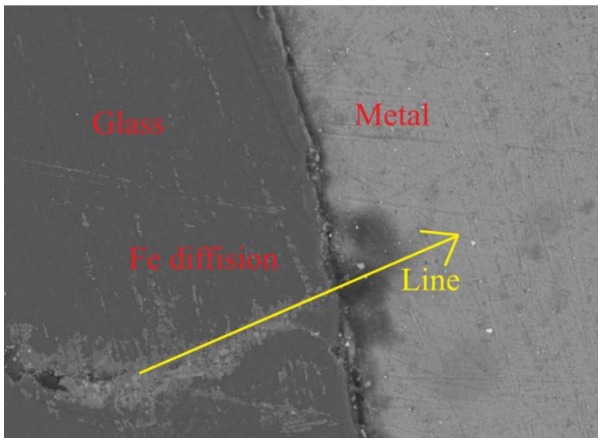

Figure 1. GTM interface for A-4 glass with a sealing profile at temperatures of 950 and 450 °C at X5000.

Figure 5 shows the EDS analysis results taken along the yellow line in Figure 4. The EDS analysis was performed along the line to examine all temperature profiles. As seen in this figure, Fe ions are present inside the glass.

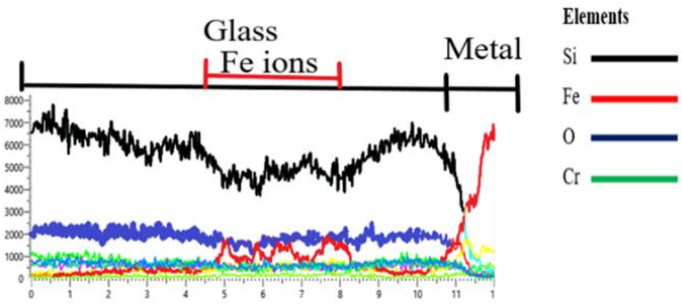

Figure 5. GTM interface EDS analysis for A-4 glass with a sealing profile at temperatures of 950 and 450 °C.

Even though the Fe ions inside the glass are clearly visible, is not any dendric structure like the one seen in the sealing profile at temperatures of 950 and 450 °C. This sealing profile shows weak Van der Waals bonds. However, Fe ions are detected inside the glass in sealing profile at temperatures of 980 and 480 °C, shown in Figure 6 so, it has strong chemical bonds.

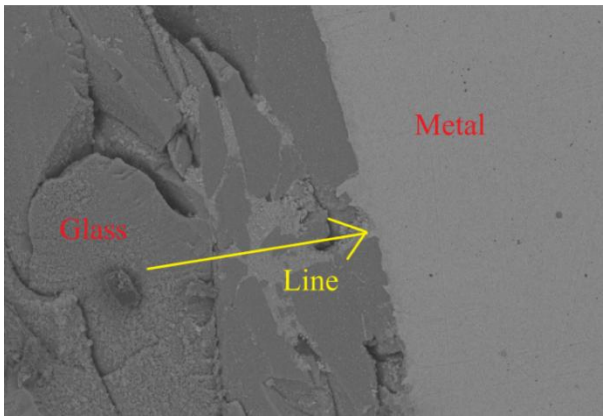

Figure 6. Glass metal interface for A-4 glass with a sealing profile at temperatures of 980 and 480 °C at X3000.

Even though other sealing profiles can be used for sealing of A-4 glass, sealing profile at temperatures of 950 and 450°C offer the best features for A-4 glass. This sealing profile demonstrates a mechanical bond, supported by Fe diffusional areas and chemical bonds supported with saturated Fe ions at the GTM interface.

3.2 Sealing Results for A-1, A-2, A-3 Glasses

Although A-4 glass demonstrated the best microstructural features compared to the other glasses, A-1, A-2, and A-3 glasses were sealed with 304 SS using a sealing profile at temperatures of 980 and 480 °C. This profile selection was based on the Tg of the glasses. The Tg of A-1 glass is higher than 450 °C. Therefore, 480 °C was selected as the second temperature for sealing, for all glasses.

Figure 7 depicts the sealing interface for A-1 at the sealing profile at temperatures of 980 and 480 °C. The diffusion of Fe ions into the A-1 glass, particularly within the interface region enriched with Fe ions. Hence, A-1 glass, and 304 SS has mechanical bonds. Throughout the interface between them, there are some diffusional regions. For A-1 glass, this sealing profile is sufficient. Thanks to that interface is saturated by Fe.

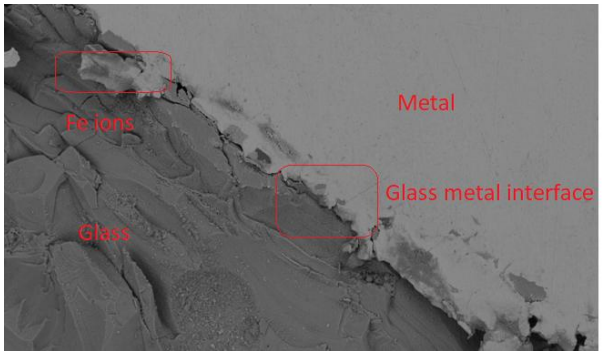

Figure 7. GTM interface for A-1 glass with a sealing profile at temperatures of 980 and 480 °C at X1000.

Figure 8 shows the A-2 sealing interface and EDS results. According to the line EDS analysis indicates nearly sharp elemental changes. However, there is no evidence of Fe diffusion through the A-1 glass. Thus, strong bonds could not be detected due to the non-presence of Fe in the A-2 glass.

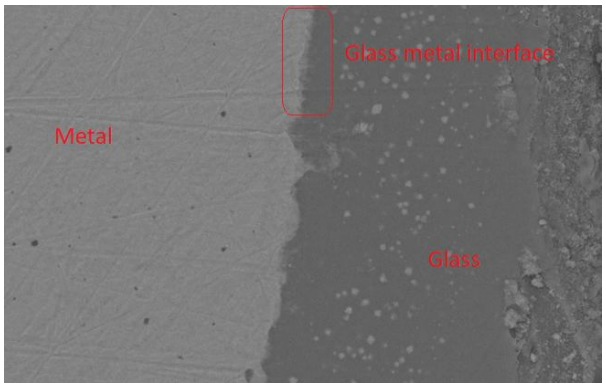

Figure 8. GTM interface for A-2 glass with a sealing profile at temperatures of 980 and 480 °C at X8500.

Figure 9 depicts the A-3 glass sealing interface and EDS results for the sealing profile at temperatures of 980 and 480 °C. According to the microstructure of the interface and EDS results for A-3 glass, it is evident that there are strong mechanical and chemical bonds at the interface.

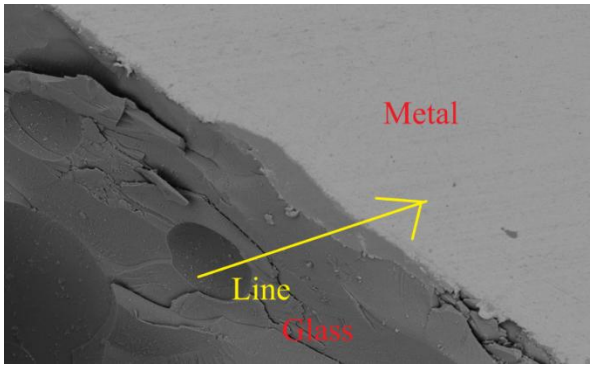

Figure 9. GTM interface for A-3 glass with a sealing profile at temperatures of 980 and 480 °C at X1000

Cr ions diffusional region at the A-3 glass and metal interface is indicated by Figure 10. Other studies have observed Cr and Fe ions at the GTM interface [13,14]. However, in those studies, the metal was subjected to a pre-oxidation process before the sealing procedure, which enabled the adhesion between the glass and metal through the oxide layer. The presence of Cr and Fe at the interface in A-3 glass could be due to an oxide layer formed during the sealing process. Additionally, this oxide layer may contribute to the chemical bonding between the glass and metal [12].

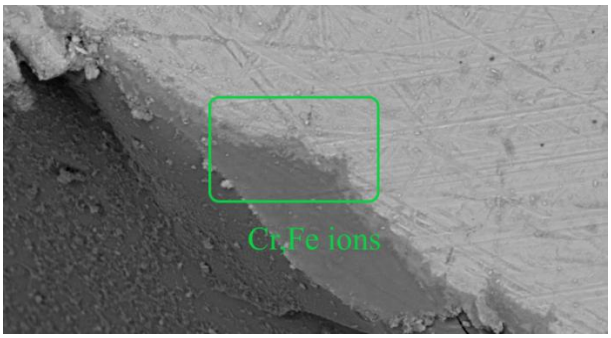

Figure 10. GTM interface with Cr and Fe diffusion for A-3 glass at X6000.

4. Conclusion

To sum up, the changes in the glass's properties, such as density, Tg, chemical durability, and CTE, as influenced by the Na_2O/K_2O ratio of alkali barium glasses. In additionally, the microstructure developed between 304 SS and glass is also affected by both the sealing profiles and the Na_2O/K_2O ratios of the glass.

Even A-3 glasses form strong chemical bonds with the sealing profile at temperatures of 980 and 480 °C, thanks to the presence of Cr. A-4 glasses can seal with 304 SS using different sealing profiles, resulting in strong bonds. A-4 glass exhibits the most favorable sealing interface with a sealing profile at temperatures of 950 °C and 450 °C, which is attributed to the saturated interface formed by Fe and its bonding with the glass region.

Authors' Contributions

Declaration of Competing Interest

The authors declare that they have no known competing financial interests or personal relationships that could have appeared to influence the work reported in this paper.

Acknowledgement

I would like to thank TÜBİTAK SAGE, who provided financial and technical device support for this research.

References

[1] R. R. Tummala, E. J. Raymaszewski, and A. G. Klopfenstein, "Hermetic Versus Non-Hermetic Packaging, Types of Hermetic Packaging," Microelectronics Packaging Handbook Semiconductor Packaging, 1996, pp. 876–907.

[2] R. M. Rulon, "Glass to metal seals," Introduction to Glass Science, pp. 661–704, 1972.

[3] "Controlled Expansion Metal Alloys: Kovar, molybdenum, Alloy 52," Nealloys, [Online]. Available: https://www.nealloys.com/pdf. [Accessed: Jan. 12, 2024].

[4] M. J. Pascual, "Glasses and glass-ceramics as sealing materials," in Encyclopedia of Materials: Technical Ceramics and Glasses, vol. 2–3, Elsevier, 2021, pp. 746–761.

[5] P. Pham, P. Goel, S. Kumar, and K. Yadav, "Wettability on Different Surfaces," in 21st Century Surface Science: A Handbook, London: Intech Open, 2020, pp. 115–128.

[6] J. E. Shelby, "Principle of Glass Formations, Structures of Glass, Density and Thermal Expansion," Introduction to Glass Science and Technology, Royal Society of Chemistry, 2005.

[7] R. Rajaramakrishna and J. Kaewkhao, "Glass material and their advanced applications," Social Sciences, 2019.

[8] R. H. Dalton, "Solder glass sealing," Journal of the American Ceramic Society, vol. 39, no. 3, pp. 109–112, 1956.

[9] B. W. King, H. P. Tripp, and W. H. Duckworth, "Nature of adherence of porcelain enamels to metals," Journal of the American Ceramic Society, vol. 42, no. 11, pp. 504–525.

[10] S. Englise and W. E. Turner, "Relationship between chemical composition and the thermal expansion of Glasses," Journal of the American Ceramic Society, vol. 10, no. 8, pp. 551–560.

[11] S. Sen and F. V. Tooley, "Effect of Na2O/K2O ratio on chemical durability of alkali-lime-silica glasses," Journal of the American Ceramic Society, vol. 38, no. 5, pp. 175–177, 1955.

[12] I. W. Donald, B. L. Metcalfe, and L. A. Gerrard, "Interfacial reactions in glass-ceramic-to-metal seals," Journal of the American Ceramic Society, Mar. 2008, pp. 715–720.

[13] L. Peng, Q. Zhu, Z. Xie, and P. Wang, "Interface Reactions Between Sealing Glass and Metal Interconnect Under Static and Dynamic Heat Treatment Conditions," J. Fuel Cell Sci. Technol., vol. 12, no. 6, Dec. 2015, doi: 10.1115/1.4032337.

[14] S. Li, Y. Cai, Q. Zhu, Z. Liu, and Y. Zhang, "Interface degradation of glass-to-metal seals during thermo-oxidative aging," Corrosion Science, vol. 199, p. 110189, 2022, doi: 10.1016/j.corsci.2022.110189.

BMSM

Bulletin of Materials Science & Metallurgy

Periodical Scientific Journal of UCTEA Chamber of Metallurgical and Materials Engineers

Volume 1, Issue 3, 2024, Pages 25-30 Received: 15 November 2024 Accepted: 25 December 2024

https://doi.org/10.70342/QYXE2962

Research Article

Effect of Aluminum Content on the Properties of Spark Plasma Sintered Tungsten, Niobium, Vanadium, Molybdenum & Aluminum Refractory High Entropy Alloys

Erman Yaman[a,*], Duygu Ağaoğulları[a] and M.Lütfi Öveçoğlu[a]

[a]Istanbul Technical University

*Corresponding author's email: erman.yaman@tubitak.gov.tr

Abstract

Four samples with 6 hours MA durations were prepared with the Al concentrations of 0.25, 0.5, 0.75 and 1 for spark plasma sintering. XRD analysis for both pre-sintered and sintered samples showed single BCC phase. Equiaxed grain morphology and homogenous distribution of the elements were detected by SEM/EDS investigations. Highest hardness value was acquired as 1.5 GPa from Al 0.5 M sample.

Keywords

High Entropy Alloys, Refractory, Composites, Metals, Multi-metallic Cocktails

1. Introduction

High entropy alloys (HEAs) have created an important paradigm shift and change in alloy design processes. In recent years, new HEAs based on refractory elements have been geared towards high temperature applications. Refractory high entropy alloys (RHEAs) are materials that have superior high temperature properties (above 800°C) such as strength and hardness [1-2], resistance to oxidation, wear and corrosion [3-5]. Even some RHEAs can maintain strength values up to 1600°C [6-7]. These exceptional features are in high demand in the aviation and aerospace industries as load-bearing or thermal protection structures.

Conventional synthesis methods of RHEAs are primarily focused on vacuum arc-melting, which produces dendritic microstructures and coarse grain size, resulting in undesirable final properties. In recent years, mechanical alloying (MA) has emerged as a superior technique over vacuum arc melting for the synthesis of refractory high entropy alloys due to several key advantages. Firstly, mechanical alloying allows for the production of RHEAs with a greater variety of compositions and alloying elements [8]. Secondly, mechanical alloying offers excellent homogeneity at the atomic level, resulting in a more uniform distribution of alloying elements in the microstructure of RHEAs which enhances the overall mechanical properties, such as hardness and tensile strength of the final alloy [9-10]. Furthermore, mechanical alloying promotes the formation of metastable phases and solid solutions, which are desirable for the development of novel RHEAs with enhanced properties. The high-energy milling involved in mechanical alloying induces severe plastic deformation and facilitates the synthesis of new phases, leading to improved mechanical and thermal stability. [11-12].

The combined utilization of mechanical alloying and spark plasma sintering (SPS) has shown great potential in the development of RHEAs with exceptional properties. Recent studies have focused on exploring the synergistic effects of these techniques to tailor the microstructure and enhance the mechanical and thermal properties of refractory alloys. Mechanical alloying, through high-energy ball milling, promotes the formation of nanocrystalline structures and the homogeneous distribution of multiple principal elements in near-equimolar ratios. Subsequently, spark plasma sintering facilitates the rapid consolidation of mechanically alloyed powders, resulting in fully dense alloys with refined microstructures and improved mechanical properties. The combined approach has demonstrated promising results in the development of RHEAs based on tungsten (W) combined with elements such as molybdenum (Mo), niobium (Nb), vanadium (V), and aluminum (Al). These alloys exhibit enhanced strength, excellent thermal stability, and improved resistance to wear and corrosion. The MA-SPS combination has proven successful in achieving controlled phase formation, homogeneous mixing, and the preservation of nanoscale features, enabling the production of high-performance refractory alloys for applications in extreme temperature environments [1-2-3].

In this present work, concept of RHEA was tested by spark plasma sintering W, Nb, V, Mo refractory elements and generating HEA with an addition of Al element to achieve better mechanical properties and homogeneous distribution of the elements. Four samples were produced and seperated among each other for their Al concentrations. The produced samples are as follows; 6 hours MA'd $WNbMoVAl_x$ where x is, 0.25, 0.5, 0.75 and 1. MA duration of 6 hours was selected as the optimum time since from the literature it was obtained that 2 hours of mechanical alloying causes elemental powders to finally dissolve into crystal structures with single phases, 4 hours and 6 hours are the critical durations for mechanical alloying since single-phase crystal structures complete their formation. However, beyond 6 h mechanical alloying, it was observed that fine particles obtained by mechanical alloying may start to agglomerate and form coarser particles [10].

2. Experimental Procedure

The starting materials used in this investigation were high purity (> 99.6 %) W (supplied from AEM™, particle size < 45 microns), Mo, Nb and V (supplied from Jinzhou Haixin Metal Materials™ Co. Ltd., particle size < 10 microns) and Al powders. Two groups of powder samples were blended, each blend weighing 12 g. The experimental group is constituted of equimolar amounts of the refractory elements, whereas the amount of Al is increased systematically from zero to equimolar and is referred to as $WNbMoVAl_x$ (x = 0, 0.25, 0.50, 0.75 and 1.0). Powder batches were mixed in a WAB™ T2C Turbula mixer for about 1 h. WC vials and WC balls were cleaned with isopropyl ethanol and the pre-cleaned WC vials and milling balls were coated with equimolar WNbMoV powders via mechanical alloying for 4 hours before each process to further reduce the chances of contamination. After that, the prepared powder mixtures were placed in pre-cleaned WC vials (50 ml) with WC balls and the filled vials were closed and sealed under high purity Ar (Linde™, 99.999%) atmosphere in a MBraun™ glove box. Care was taken to ensure that the O_2 and humidity inside the glove box did not exceed 50 ppm and 1 ppm, respectively. Mechanical alloying experiments were carried out with a ball-to-powder (BPR) weight ratio of 10:1 with the duration of 6 h in a Spex™ 8000D dual mill rotated at 1200 rpm. Mechanically alloyed samples were spark plasma sintered at 1500^0C under 35 MPa pressure for 10 minutes in a FCT™ GmbH brand HPD-50 model SPS furnace. The density values of both the MA'd and SPS'd samples were tested by Archimedes' principle. Vickers hardness tests of both MA'd and SPS'd samples were carried out in a Shimadzu™ HMV microhardness tester. A total of 25 indentations were taken from the samples at 8 different corner and edge locations using a load of 9 N for 15 seconds.

In order to determine the phase characteristics of the $WNbMoVAl_x$ (x = 0, 0.25, 0.50, 0.75 and 1.0) refractory high entropy alloys, CALPHAD FactSage™ 7.2 simulation program was used. The correlation of the simulation data and the experimental data was tested via XRD for both mechanically alloyed and spark plasma sintered samples. From the simulation, it is deduced that the addition of Al atoms increases the BCC2 phase and elevates the BCC transformation temperature of this phase to 1000^0C. As the incremental addition of Al atoms increases, the formation of intermetallic compounds of $AlMo_3$, Al_3Nb, and Al_8Mo_3 are predicted to emerge. X-ray diffractometry (XRD) and scanning electron microscopy (SEM) investigations were carried out to characterize the MA'd and SPS'd refractory high entropy alloy samples. A Bruker™ D8 Advanced Series X-ray diffractometer was operated to identify the crystalline phases using CuKα (λ = 1.5406 Å) radiation (0.154 nm, 35 kV, 40 mA) with a scanning speed of 2/min. Microstructural characterizations and spectral chemical analyses of the MA'd and SPS'd RHEAs were carried out using a Thermo Scientific Quattro scanning electron microscope (15 kV) coupled with an energy-dispersive X-ray spectrometer (EDX).

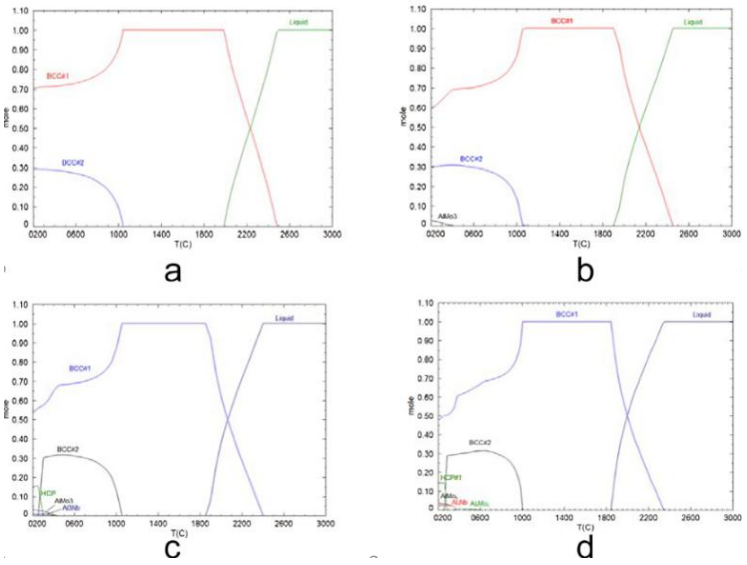

Figure 1. Phase formation diagrams by CALPHAD model for a)$Al_{0.25}WNbMoV$, b)$Al_{0.5}WNbMoV$,c)$Al_{0.75}WNbMoV$, d)$AlWNbMoV$ compositions.

Particle sizes were measured in deionized water media using a Malvern™ Laser particle size analyzer (PSA). Before the PSA analysis, powders in distilled water were dispersed using a Bandelin Sonopuls™ ultrasonic homogenizer.

3. Results and Discussion

3.1. Characterization of the powders

Figures 2a and 2b show the particle size distributions of the equimolar WVMoNbAl RHEA powders MA'd for 2 h and 6 h, respectively. It can be deduced that as the MA duration increases, the particle sizes of the MA'd RHEA powders decrease. Further, the 6 h MA'd sample displays a Gaussian-like average particle size distribution.

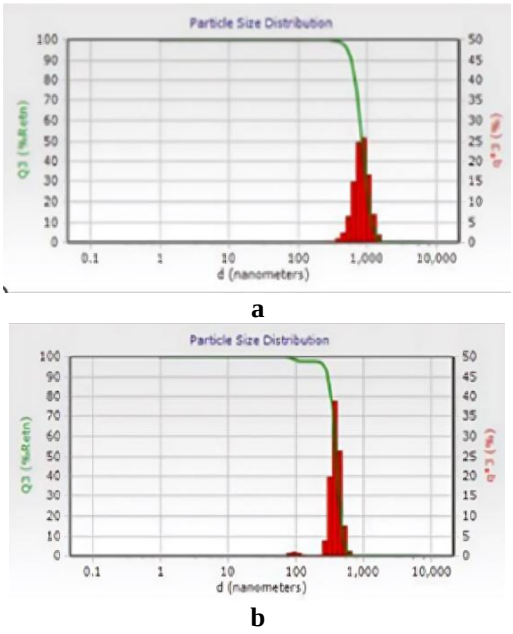

Figure 2. Particle size distributions of the equimolar WVMoNbAl refractory high entropy alloy: a) MA'd for 2 h and b) MA'd for 6 h.

In the light of the particle size distributions 6 h was selected as the optimum MA duration for further investigations prior to consolidation.

XRD patterns of $WVMoNbAl_x$ refractory high entropy alloy were investigated for their different compositions. Figure 3, shows the XRD patterns for, 0.5, and 1 Al mole fractions having $WVMoNbAl_x$ refractory high entropy alloys for MA durations of 6 hours. It is important to note that these patterns belong to the samples which are mechanically alloyed and spark plasma sintered. Single BCC dominant phase was observed with some minor carbide phases which is most likely the result of MA and/or SPS processes.

Density and hardness measurements were conducted on the spark plasma sintered $WVMoNbAl_x$ RHEA samples. For different Al concentrations the theoretical density, experimented density and relative density values were given in **Error! Reference source not found.**. The experimental density values were gauged with Archimedes' method by weighting the samples in air and water settings. It can be deduced that the porosity amount of $WVMoNbAl_x$ RHEAs produced by mechanical alloying and spark plasma sintering methods within the scope of the experiment is less than 15%. Porosity values may depend on many factors, such as external gases that have not been sufficiently cleaned in the vacuum chamber before mechanical alloying, insufficient mechanical alloying.

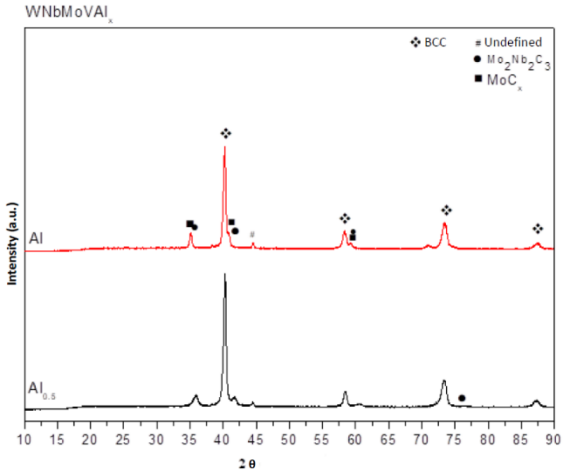

Figure 3. XRD patterns of SPS'd $WVMoNbAl_x$ refractory high entropy alloy with 6 hours of mechanical alloying and 0.5, 1 molar Al concentrations.

Considering these conditions, it is not possible to reach a definite conclusion about the measured densities and mechanical alloying times of the tested compositions. However, with the increase of aluminum concentration, the overall density of the sample decreases as expected, since the density values of the MA'd and spark plasma sintered, WVMoNb powders showed higher Archimedes density values which are; 10.11, 10.45, 10.81, 10.24, 10.34 g/cm^3 respectively.

3.2. Mechanical properties

Vickers hardness values of mechanically alloyed and spark plasma sintered, at 1500^0C, under 35 MPa for 10 minutes, samples were tested and compared according to their Al concentrations. **Error! Reference source not found.**1, shows the Vickers hardness values, along with the relative densities of each alloy tested through this research.

From the data given it can be deduced that the increasing addition of Al element increases the hardness value of the samples. This depiction is based on the comparison of these samples among each other and with the WNbMoV alloys from the literature [5]. Solid solution hardening along with the severe lattice distortion caused by the Al atoms, as well as the BCC stabilizer effect causes hardening on the alloys and finer grain sizes with the increased MA durations are the mechanisms behind the hardness results [10-11-12]. The Vickers hardness values of $WVMoNbAl_x$ RHEAs samples at various aluminum concentrations were obtained by hardness tests under a 9 N load for 15 seconds and performed at an average of 25 different points for each sample. In the light of the results obtained, it was concluded that the solid solution hardening mechanism was effective as a result of the addition of aluminum to the sample [11-12].

Table 1. Vickers hardness and relative density values of SPS'd $WVMoNbAl_x$ RHEA for different Al concentrations. (a: non-SPS'ed)

Alloy	MA Duration	Relative % Density	Hardness (GPa)	Standard Deviation
$WVMoNbAl_{0.25}$	6 hours	89.40	13.6	0.72
$WVMoNbAl_{0.5}$	6 hours	90.39	15.0	0.676
$WVMoNbAl_{0.75}$	6 hours	98.66	14.11	0.61
WVMoNbAl	6 hours	90.30	12.31	0.86
WVMoNbAl	0 hours	89.15	7.65	0.94
WVMoNbAl[a]	6 hours	60.31	-	-
WVMoNbAl[a]	8 hours	62.66	-	-

These results became especially predominant when compared with the WVMoNb base alloy, since the base alloy with 6 hours MA duration had hardness value of 11.74 GPa, which was previously determined within the scope of TÜBİTAK 119M980 project, conducted by ITU PML.

Aluminum atoms cause distortions in the lattice structure after finding a place for themselves among the crystal structure formed by the base alloy elements in the quaternary system [11-12-13]. Dislocation movements are restricted due to the escalation of lattice potential resulting in an increment in material hardness and strength [11-12-13]. When the hardness values of the samples were compared, it was observed that the highest hardness value was obtained for the RHEA containing 0.5 Al. It was clear that the effect of SPS on the hardness values of the samples was undeniable.

Wear tests were carried out with the parameters of 4 N load, 2 mm length, 6 mm/s sliding speed for 50 meters. 6 mm Al_2O_3 balls were used as a counterface. Data for friction coefficients, wear track areas, and wear rate were gathered and represented in Table 2. When the data from the table is examined, 6 hours and 8 hours of mechanically blended samples yield very close values, and comparison between 0.5 Al and 1 Al can be observed. Mechanical alloying duration along with Al content has a positive effect on wear properties of the RHEA.

Table 2. Volume losses and wear rates of $WMoNbVAl_x$ RHEA samples.

Alloy	MA Duration	Wear Track Area (mean, nm^2)	Wear Rate (mm^2/N)
WVMoNbAl	2 hours	74.3	$0{,}74x10^{-15}$
WVMoNbAl	6 hours	34.8	$0{,}348x10^{-15}$
WVMoNbAl	8 hours	32.7	$0{,}32x10^{-15}$
$WVMoNbAl_{0.5}$	6 hours	85.67	$0{,}85x10^{-15}$

3.3.Microstructure

SEM/EDS analyses of the samples show the distribution of the elements throughout the alloy. From the Fig4, the as-blended samples grain morphology can be observed. The dark and light grey phases seen in the 2000x magnification image are the phases where the main matrix and the tungsten rich areas are dense respectively. The dark grey areas are the BCC matrix phases and the light grey areas are WC-rich areas. When the overall composition of the sample was taken into consideration, the amount of light grey areas is very low that it can be neglected.

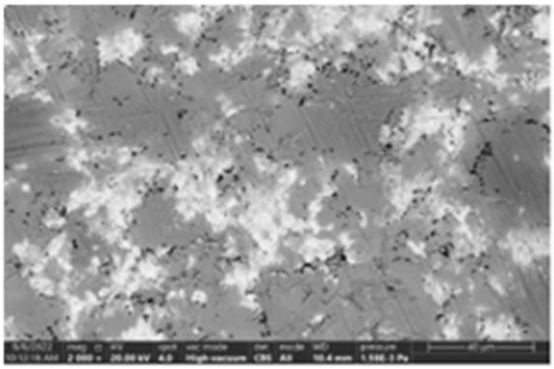

A

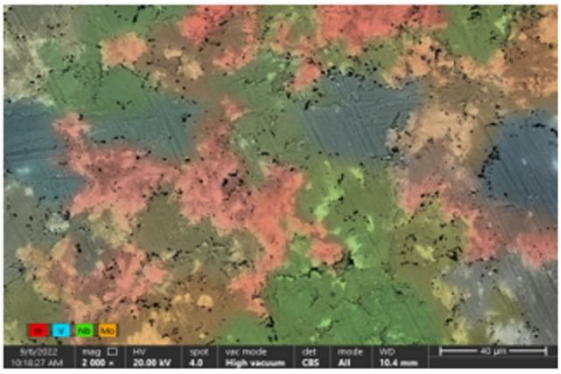

B

Figure 4. As-blended, spark plasma sintered, equimolar WVMoNbAl RHEAs 2000x EDS/SEM mappings.

When the EDS analyzes are examined from the Figure5, it can be said for the 0.25 M, 6 h MA'd sample, it has a largely homogeneous element distribution as it is shown in **Error! Reference source not found.**3. It can be deduced that with MA duration, the alloy becomes more homogenously distributed and grain size is reduced.

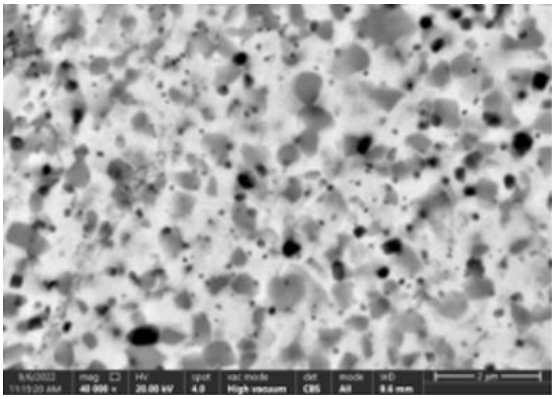

A

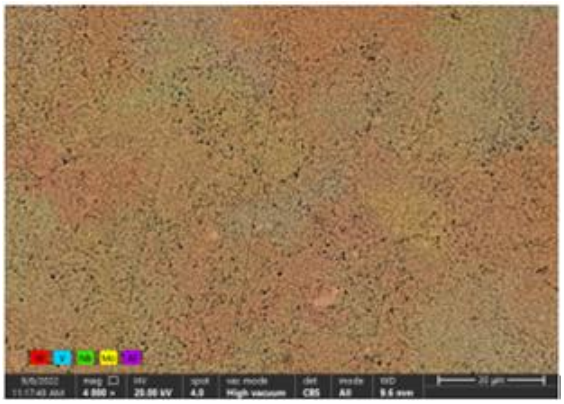

B

Figure 5. Images of 0.25M $WVMoNbAl_x$ RHEA with 6 hours MA duration a)40000x b)4000x EDS/SEM.

Table 3. Elemental distribution of the $WVMoNbAl_x$ RHEA with 0.25 Al concentration and 6 hours MA duration.

Alloy	Atomic %	Atomic % Error	Weight %	Weight % Error
Al	5.9	0.2	1.6	0.0
V	23.3	0.1	11.6	0.0
Nb	26.1	0.6	23.8	0.6
Mo	20.6	0.0	19.4	0.0
W	24.2	0.2	43.6	0.3

4. Conclusion

In this work, a total of 8 $WVMoNbAl_x$ refractory high entropy alloys were produced using mechanical alloying and spark plasma sintering techniques at different Al concentrations (0.25, 0.5, 0.75, and 1.0 wt.%), followed by their characterization investigations and mechanical tests. The effects of the Al element on the properties of the produced RHEA were investigated.

On the basis of the results reported in work, the following conclusions can be drawn:

From the data retrieved from the literature, 6 hours of mechanical alloying duration was found to be the optimum duration for the alloying process. Hardness tests were carried out under a 9 N load for 15 seconds and 25 tests from different points were operated for each sample. These results have indicated the increases in hardness values of the $WVMoNbAl_x$ can be attributed to increased MA duration and Al concentration (to a certain extent). The highest hardness values of 15 GPa and 14.11 GPa belong to the $WVMoNbAl_x$ (x=0.5, 0.75) RHEA samples mechanically alloyed for 6 hours, respectively. From the results it can be inferred that Al atoms trigger the solid solution hardening mechanism in the alloy by merging into the lattices, causing distortions and preventing dislocation movements leading to increased hardness of the alloys. Wear test data shows that, 6 hours and 8 hours of mechanically blended samples yield very close values, and comparison between 0.5 Al and 1 Al can be observed. Mechanical alloying duration along with Al content has a positive effect on wear properties of the RHEA.

Microstructures and elemental distribution of the samples were investigated. Almost every sample had a homogenous distribution of the elements throughout the alloy. The as-blended sample had the least homogenous distribution of the elements compared to the other samples, proving the effect of MA on elemental distribution. Overall, the observed phase was the single BCC phase for spark plasma sintered samples. The scanning electron microscope images showed three distinct regions on them, color-coded as; light grey, dark grey, and black regions. Those regions were composed of tungsten-rich, BCC matrix, and porosities. Therefore, SEM images of the samples are coherent with the XRD patterns of the samples.

Authors' Contributions

Project administration: Duygu Ağaoğulları, M. Lütfi Öveçoğlu; Supervision: Duygu Ağaoğulları, M. Lütfi Öveçoğlu; Writing-original draft preparation: Erman Yaman, M. Lütfi Öveçoğlu; Writing-review and editing: M. Lütfi Öveçoğlu; Conceptualization: Duygu Ağaoğulları, M. Lütfi Öveçoğlu; Investigation: Erman Yaman

Declaration of Competing Interest

The authors declare that they have no known competing financial interests or personal relationships that could have appeared to influence the work reported in this paper.

Acknowledgement

This study is a part of a research project entitled "Synthesis of refractory high entropy $WNbMoVCr_xAl_y$ (x, y = 0 - 1,0) alloys via mechanical alloying, their densification and sintering using various processes and related characterization investigations" funded by the Technological and Research Council of Turkey (TÜBİTAK) with a project number of 119M980 and this is greatly appreciated. We would like to thank Prof. Dr. Hüseyin Çimenoğlu for allowing us to access his laboratory facilities and Mertcan Kaba in carrying out the wear tests. Additionally, we want to thank Assoc. Prof. Dr. Erhan Ayas and Kübra Gürcan Bayrak at Eskişehir Technical University for performing the spark plasma sintering experiments and Assoc. Prof. Dr. Bedri Baksan at Osmangazi University for the high temperature compression tests of the present study.

References

[1] Senkov, O.N., Wilks, G.B., Miracle, D.B., Chuang, C.P., Liaw, P.K. 2010. "Refractory high-entropy alloys", Intermetallics, 18, 1758-1765.
[2] Kim, H., Nam, S., Roh, A., Son, M., Ham, M., Kim, J., Choi, H. 2019. "Mechanical and electrical properties of NbMoTaW refractory high-entropy alloy thin films", International Journal of Refractory Metals and Hard Materials, 80, 286-291.
[3] Senkov, O. N., Senkova, S.V., Dimiduk, D. M., Woodward, C., Miracle, D. B. 2012. "Oxidation behavior of a refractory $NbCrMo_{0.5}Ta_{0.5}TiZr$ alloy", J. Mater. Sci., 47, 6522 – 6534.
[4] Poulia, E., Georgatis, E., Lekataou, A., Karantzalis, A. E. 2016. "Microstructure and wear behavior of a refractory high entropy alloy, Int. J. Refrac. Met. Hard Mater., 57, 59 – 63.

[5] Jayaraj, J., Thinaharan, C., Ningshen, S., Mallika, C., Kamacci, M. 2017., "Corrosion behavior and surface film characterization of TaNbHfZrTi high entropy alloy in aggressive nitric acid medium, Intermetallics, 89, 123 – 132.
[6] Senkov, O.N., Wilks, G.B., Scott, J.M., Miracle D.B. 2011. "Mechanical properties of $Nb_{25}Mo_{25}Ta_{25}W_{25}$ and $V_{20}Nb_{20}Mo_{20}Ta_{20}W_{20}$ refractory high entropy alloys", Intermetallics, 19, 698-706.
[7] Senkov, O. N., Senkova, S.V., Miracle, D.B.,Woodward, C. 2013. "Mechanical properties of low-density, refractory multi-principal element alloys of the Cr–Nb–Ti–V–Zr system", Materials Science & Engineering A, 565, 51-62.
[8] Senkov, O.N., Miracle, D.B., and Woodward, C.F. (2011). "Mechanical alloying and milling", Progress in Materials Science, 56(2), 284-327.
[9] Guo, S. (2013). "Phase formation and mechanical properties of high-entropy alloys", Progress in Materials Science, 61, 1-93.
[10] Torabi, O., et al. (2015). An investigation on the formation mechanism of nano CrB2 powder in the Mg–B2O3–Cr2O3 system. *International Journal of Refractory Metals and Hard Materials, 51*: 50-55. https://doi.org/10.1016/j.ijrmhm.2015.02.015
[11] D. Zhang, et al. (2022). Mechanical alloying and spark plasma sintering of high entropy refractory alloys: A review. Journal of Materials Science & Technology, 100, 227-242.
[12] Y. Liu, et al. (2022). Microstructure and properties of mechanically alloyed and spark plasma sintered refractory high entropy alloys. Materials Letters, 317, 130462.
[13] Z. Wang, et al. (2023). Synergistic effects of mechanical alloying and spark plasma sintering on the microstructure and properties of high entropy refractory alloys. Journal of Alloys and Compounds, 895, 162375.